Growing stripes, with and without wrinkles*

M. Avery[†], R. Goh[‡], O. Goodloe[§], A. Milewski[¶], and A. Scheel[‖]

Abstract. We present results on stripe formation in the Swift-Hohenberg equation with a directional quenching term. Stripes are "grown" in the wake of a moving parameter step line, and we analyze how the orientation of stripes changes depending on the speed of the quenching line and on a lateral aspect ratio. We observe stripes perpendicular to the quenching line, but also stripes created at oblique angles, as well as periodic wrinkles created in an otherwise oblique stripe pattern. Technically, we study stripe formation as traveling-wave solutions in the Swift-Hohenberg equation and in reduced Cahn-Hilliard and Newell-Whitehead-Segel models, analytically, through numerical continuation, and in direct simulations.

Key words. Swift-Hohenberg, Cahn-Hilliard, stripe selection, zigzag instabilities, growing domains

AMS subject classifications. 35B36, 37C29, 35B32

1. Introduction.

Striped phases appear in a plethora of contexts, from sand [46] and icicle ripples [4], to convection roll [3] and precipitation patterns [49], to bacterial colony growth [2] or the formation of presomites in early development [45], and to ion-beam milling [30], dip-coating [52], lamellar crystal growth [7, 1], and water jet cutting [12]. Simple understanding of such patterns is often based on the weak instability of a trivial, spatially constant state against perturbations that are periodic in space with wavenumbers close to a critical wavenumber $k_\mathrm{c} > 0$. While the selection of this specific wavenumber may be due to quite different and complex physical mechanisms, the resulting phenomena, at least for weak instabilities, often bear a striking resemblance. In many cases, phenomena are well captured by simple, universal models such as the Swift-Hohenberg equation [47],

$$u_t = -(1+\Delta)^2 u + \rho u - u^3 \tag{1.1}$$

posed on $(x, y) \in \mathbb{R}^2$, with $0 < \rho \ll 1$. The linear part will enhance Fourier modes $\mathrm{e}^{\mathrm{i}(k_x x + k_y y)}$ with $k = \sqrt{k_x^2 + k_y^2} \sim k_\mathrm{c} = 1$, and the nonlinear part leads to (local) saturation and competition of these modes, such that the locally dominant observed pattern is of the form $\mathrm{e}^{\mathrm{i}(k_x x + k_y y)} + c.c.$, $k \sim 1$, for some orientation of the wave vector (k_x, k_y) depending on space (x, y). Indeed, starting the system with random initial conditions in a large domain leads to quite complex, incoherent structures; see Fig. 1. One mostly observes such sinusoidal stripe patterns with some locally chosen orientation, but these local stripe domains are bordered by a plethora of defects, including grain boundaries, dislocations, and disclinations [33].

*Submitted to the editors February 19, 2019.
Funding: This work was partially supported by NSF grants DMS–1612441 (AS) and DMS–1603416 (RG).
[†]University of Minnesota, Minneapolis, MN (avery142@umn.edu)
[‡]Boston University, Boston, MA (rgoh@bu.edu)
[§]Arizona State University, Tempe, AZ (ogoodloe@asu.edu)
[¶]University of Bristol, Bristol, UK (am16053@my.bristol.ac.uk)
[‖]University of Minnesota, Minneapolis, MN (scheel@umn.edu,www.umn.edu/~scheel)

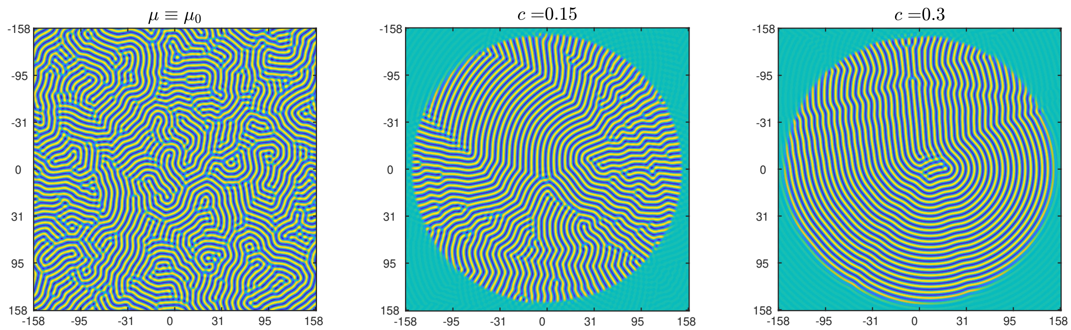

Figure 1. *Patterns in (1.1) from random initial conditions with $\rho \equiv 0.25$ (left), compared to results from directional quenching $\rho = 0.25\mathrm{sign}(ct - |(x, y)|)$ (center, left). Note the orientation of stripes predominantly parallel to the quenching boundary for the large speed and wrinkly structures for the smaller speed.*

Directional quenching. Such a spatially constant unstable state is sometimes obtained via a quenching process, where system parameters are changed in the whole system rapidly, rendering a spatially constant state unstable. In phase separating systems, this typically refers to a rapid cooling from a stable state of well mixed phases to a regime where phases separate. In many of the physical contexts listed above, patterns do not arise through such a spatially homogeneous quenching process, but one rather observes that the domain in which patterns form grows in time. There has been quite some interest in the interplay between growth processes and pattern formation mechanisms, in particular since the phenomenology of both the growth process and the pattern formation mechanism can quite dramatically influence each other. We shall focus here on the effect of the growth mechanism on the pattern formation, and neglect the reverse effect, as a first approximation. We therefore assume that the parameter ρ in (1.1) is time- and space-dependent with $\rho = \rho(t, x, y) \equiv \mu > 0$ in a time-dependent region $(x, y) \in \Omega_t$ and $\rho(t, x, y) \equiv -\mu < 0$ in the complement $(x, y) \notin \Omega_t$. We illustrate the striking "regularity" of the resulting patterns in Fig. 1 where $\Omega_t = \{|(x, y)| < c_x t\}$ for some $c_x > 0$.

Assuming small curvature of $\partial\Omega_t$, one can think of approximating $\partial\Omega_t$ with a straight line. Assuming in addition periodicity along $\partial\Omega_t$, one is lead to consider domains $\Omega_t = \{x < c_x t|\,(x, y) \in \mathbb{R}^2\}$ with lateral periodicity $y \mapsto y + \frac{2\pi}{k_y}$, that is, growth along the axis of a laterally periodic strip. Direct simulations in this geometry, shown in Fig. 2, confirm a delicate behavior of the selection process when the transverse wavenumber k_y is close to 1 and c_x is gradually increased. Our goal is to shed light onto the complexity in this parameter regime.

Outline of phenomena. Fig. 3 presents much of the phenomenology in 50 vertically stacked simulations with increasing k_y. The speed c_x increases left to right and patterns are frozen behind the quenching line. The result gives a good illustration of the emerging patterns in the (k_y, c_x)-parameter plane. We observe stripes with different orientations relative to $\partial\Omega_t$,

- *perpendicular stripes* (horizontal in the picture),
- *oblique stripes* (slanted in the picture),
- *parallel stripes* (vertical in the picture),

and striped patterns with defects, oblique and perpendicular, respectively,

- *zigzagging stripes*,
- *spotted stripes*.

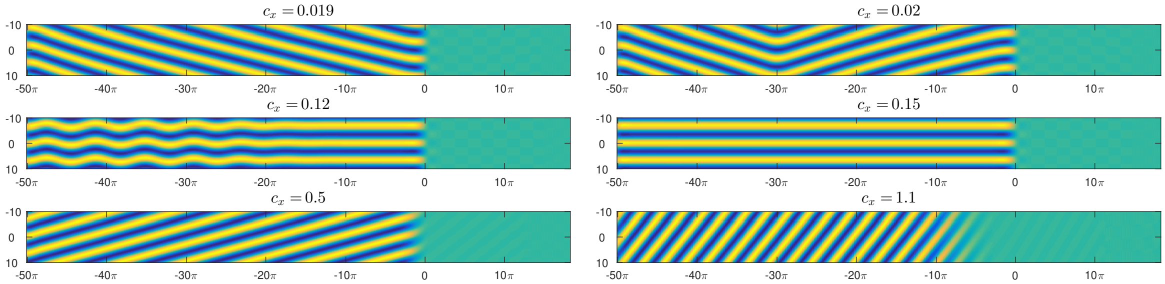

Figure 2. *Formation of striped patterns in the Swift-Hohenberg equation as analyzed and predicted, here, for* $\mu = 0.25$, $k_y = 0.95$. *Final state in simulations in a co-moving frame with quenching line at* $x = 0$. *Transitions observed (top to bottom, left to right), are from oblique to zigzag to straight, back to oblique, until stripe formation detaches.*

Increasing c_x for fixed $k_y \lesssim 1$, we observe two main transitions,

- *oblique detachment*: oblique stripes form for small speeds $c_x < c_x^{\mathrm{osn}}(k_y)$, $0.85 \lesssim k_y \lesssim 1$, until zigzagging and, for $k_y \gtrsim 0.9$, perpendicular stripes take over;
- *perpendicular detachment*: for $0.85 \lesssim k_y \lesssim 1.17$, perpendicular stripes detach at $c_x^{\mathrm{psn}}(k_y)$ and give rise to either oblique or spotted stripes.

Details of these transitions are in fact more subtle and the parameter regions visible in this figure only qualitatively reflect the more accurate analysis presented below.

An approach via modulation equations — outline of approach. Our approach here is, as a consequence, three-fold and schematically summarized in Fig. 4. In the remainder of this introduction we briefly outline strategy and results in this paper, which closely reflect the

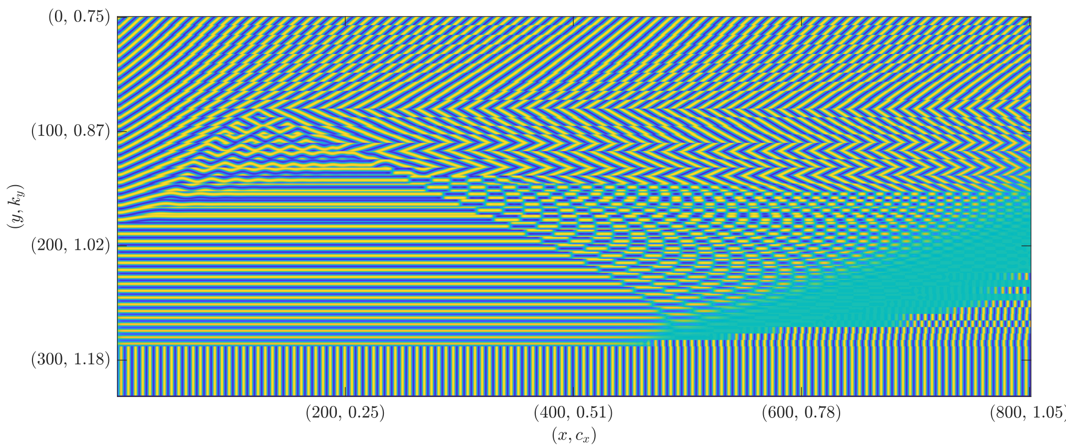

Figure 3. *Shown are 50 simulations of* (1.1) *with* k_y *varying from* 0.75 *to* 1.24 *in increments of* 0.01, *stacked vertically;* $\rho = -\frac{1}{4}\mathrm{sign}(x - \xi(t))$, *with exponential speed* $\xi(t) = 9 \cdot 10^{-5}(\mathrm{e}^{0.0013t} - 1)$. *Dynamics are frozen at* $x < \xi(t) - 10$, *such that the pattern observed at horizontal position* x *encodes the possibly transient pattern formed at the corresponding speed* $c_x \sim \xi'(t)$*; vertical position encodes values of* k_y*; see also Fig. S1 of* PARAMETER_LANDSCAPE.PDF *in the supplementary materials for more details and alternate representations with more symmetry.*

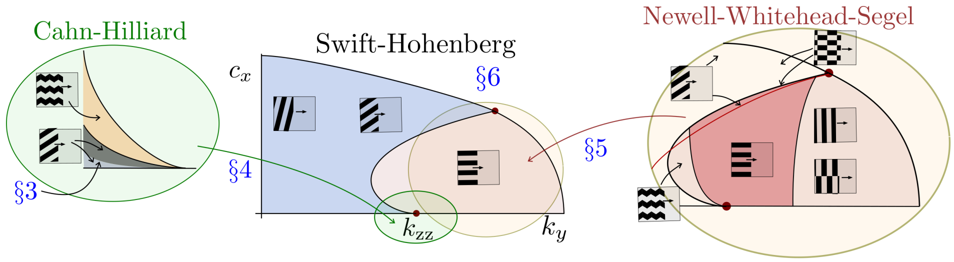

Figure 4. *Schematic illustration of results: a coarse description (center) with mostly perpendicular (light red) or oblique stripes (light blue). Details show more complexity analyzed in a Cahn-Hilliard phase approximation, §3 and §4, in a Newell-Whitehead-Segel amplitude approximation in §5, and in numerical continuation for the original Swift-Hohenberg model in §6. Note k_y is horizontal here but vertical in Fig. 3.*

organization of Fig. 4. We analyze oblique detachment in §3 and §4 within a Cahn-Hilliard phase approximation. Perpendicular detachment is analyzed within a Newell-Whitehead-Segel approximation in §5. Results are based on the description of traveling-wave solutions and their stability. The approximation by phase and amplitude equations both predicts universal validity beyond Swift-Hohenberg and makes the heteroclinic analysis more tractable. There are numerous results in the literature where validity of these modulation equations is established either for temporal dynamics or, more pertinent here, for existence and stability of particular traveling-wave solutions; see for instance [6, 44, 27, 17, 43, 20]. We shall not pursue this validation of the results obtained here for modulation equations in the Swift-Hohenberg equation, particularly since many of our results in the modulation equations are of (semi-)numerical nature. We do however compare our results with both direct simulations and computation of traveling waves in the Swift-Hohenberg equation in §6.

With the exception of the rigorous analysis of a heteroclinic bifurcation at $c_x \sim 0$ in the Cahn-Hilliard approximation that establishes existence and predicts angles for oblique stripe formation in §3, our results are stated in an informal fashion, combining numerical tools with theoretical predictions based on asymptotics near bifurcations and transitions from convective to absolute instabilities [18, 36, 34, 15]. We demonstrate that the predictions compare well with direct simulations. Making some of our predictions more rigorous poses a number of quite interesting theoretical challenges that we comment on throughout.

Oblique detachment and Cahn-Hilliard — §3 & §4. We show that phenomena for small $c_x \gtrsim 0$ and $1 - k_y = \varepsilon \sim 0$ (left panel in Fig. 4) can be captured by a Cahn-Hilliard equation with effective boundary condition

$$\psi_t = -(\psi_{xx} + \varepsilon\psi - \psi^3)_{xx} + c_x\psi_x, \; x < 0, \qquad \psi = \psi_{xx} = 0|_{x=0}\,, \tag{1.2}$$

after suitable scalings. We construct heteroclinic and homoclinic orbits for $c_x = 0$ that correspond to oblique stripes, compatible with the parameter jump (boundary condition) at $x = 0$ and analyze the singular perturbation that yields oblique stripes for $c_x \gtrsim 0$. Heteroclinic and homoclinic orbits can be understood as parts of grain boundaries, constructed in [17], and correspond in this sense quite literally to kinks (sometimes referred to as knees), where the orientation of the oblique stripe flips, or wrinkles (sometimes referred to as zigzags), where stripe orientation flips repeatedly (see Fig. 5). Our analysis predicts $\frac{\mathrm{d}k_x}{\mathrm{d}c_x}$ and agrees well with numerical results that we present later. We continue the heteroclinic profiles numerically until they disappear in a saddle-node bifurcation, the *oblique detachment*. The unstable branch corresponds to an oblique stripe that contains a kink. The saddle-node occurs when this kink detaches from the boundary, which leads to periodic kink shedding, the creation of zigzag patterns in the wake of the quenching line. The saddle-node bifurcation is of independent theoretical interest due to the presence of essential spectrum, and we discuss some interesting technical questions and phenomena in this context. We also exhibit a transition where the nature of the bifurcation changes to a hyperbolic homoclinic orbit, that causes changed asymptotics and coexistence between oblique stripes and oscillating stripe angles in large finite domains. We finally study detachment of the kink-shedding process in the Cahn-Hilliard equation, which corresponds to detachment of zigzag oscillations in Swift-Hohenberg, near a critical speed resulting in the creation of perpendicular stripes at the quenching line.

Perpendicular detachment and Newell-Whitehead-Segel — §5. We study the dynamics of stripes for moderate speeds in amplitude equations. One observes yet another saddle-node bifurcation corresponding to the *perpendicular detachment*, and an accompanying birth of a limit cycle. The bifurcation is accompanied by pitchfork bifurcations and several transitions from convective to absolute instabilities. For yet larger speeds, oblique stripes and eventually stripes of all orientations detach.

The moduli space — §6. We present computational results in the Swift-Hohenberg equation that capture oblique and perpendicular stripes, using a Newton method and farfield-core decomposition. This allows us to systematically track patterns through the saddle-node bifurcations and detect other instabilities. The results can be summarized in a surface, the *moduli space*, in the (k_x, k_y, c_x)-space. The surface is surprisingly complex. Many of the phenomena discussed here are reflected in the geometry of this surface; see Fig. 15.

Universality and similar phenomena in the literature. Directional quenching in Turing-type systems was studied qualitatively in the context of the CIMA reaction in [29], with qualitatively similar observations of transitions between parallel, oblique and perpendicular orientations. In the context of the Cahn-Hilliard equation as a model for phase separation, similar transitions have been studied in the literature. The most striking similarity can be found in a bifurcation study of a Langmuir-Blodgett transfer model [21]. Without our emphasis on a problem posed in an infinite domain, the authors observe a primary branch for small c_x (V in their notation), which destabilizes in a saddle-node bifurcation and then continues a snaking curve, different from our scenario in §3. Similar to our context, the authors do see a branch of periodic orbits limiting on the primary branch in a global homoclinic bifurcation (as in our situation, not always at the saddle-node but sometimes on a homoclinic to a hyperbolic equilibrium), which disappears in a steep Hopf bifurcation, that in the limit of large domains is caused by a detachment of kink-formation. A different scenario occurs in simple parameter triggers for Cahn-Hilliard [23], where mass conservation forces the appearance of periodic orbits for arbitrarily small speeds. A more comprehensive numerical study based on direct simulations can be found in [11]. Also, the kink-shedding process, organized by bifurcations in Cahn-Hilliard and Newell-Whitehead-Segel equations, appears to be an organizing feature behind a number of phenomena also in reaction-diffusion processes; see for instance [48, 22].

In a more narrow sense, we expect that the first part of our discussion is a universal description of growth in systems with zigzag-instabilities, since those can universally be reduced to Cahn-Hilliard type phase-diffusion problems. The second part of our analysis relies on amplitude equations and should hold quite generally near instabilities in isotropic systems that select a finite wavenumber, and in the absence of quadratic interaction terms that would favor formation of spots over stripes.

Outline. We derive modulation equations in §2, present a heteroclinic bifurcation analysis for Cahn-Hilliard in §3, and continue heteroclinics numerically in §4. We turn to Newell-Whitehead-Segel and perpendicular detachment in §5. We show computational strategies and results for Swift-Hohenberg in §6 and conclude with a discussion.

2. Zigzag instabilities and the Cahn-Hilliard approximation. We present background on zigzag instabilities in §2.1, responsible for bending and wrinkling in Fig. 2; we briefly review modulation formalism and derive the Cahn-Hilliard equation in §2.2. We also discuss spatial dynamics in this context in §2.3 and use those to motivate boundary conditions for Cahn-Hilliard on a half-line in the case of directional quenching in §2.4.

2.1. Stripes and zigzag instabilities. Striped solutions in the Swift-Hohenberg equation (1.1) can be found as particular solutions $u_\mathrm{p}(kx;k)$ of (1.1), solving

$$-\left(k^2\partial_{\xi\xi}+1\right)^2 u_\mathrm{p} + \mu u_\mathrm{p} - u_\mathrm{p}^3 = 0, \qquad u_\mathrm{p}(\xi+2\pi) = u_\mathrm{p}(\xi) = u_\mathrm{p}(-\xi),$$

It turns out that a family of such solutions bifurcates for small $\mu > 0$, for all $k \sim 1$. Since (1.1) is isotropic, we also find the associated rotated solutions $u_\mathrm{p}(k_x x + k_y y; k)$, $k = \sqrt{k_x^2+k_y^2}$. Beyond existence, one would next ask for stability of these solutions, studying the linearized operator

$$\mathcal{L}(k_x)u = -\left(k_x^2\partial_{\xi\xi} + \partial_{yy} + 1\right)^2 u + \mu u - 3u_\mathrm{p}^2(\xi;k_x)u, \qquad y,\xi \in \mathbb{R}.$$

Floquet-Bloch theory conjugates this operator to the family of operators

$$\hat{\mathcal{L}}(k_x;\sigma_x,\sigma_y)u = -\left(k_x^2(\partial_\xi + \mathrm{i}\sigma_x)^2 - \sigma_y^2 + 1\right)^2 u + \mu u - 3u_\mathrm{p}^2(\xi;k_x)u, \quad u(\xi) = u(\xi+2\pi), \tag{2.1}$$

such that the spectrum of $\mathcal{L}$ is the union of the spectra of $\hat{\mathcal{L}}(k_x;\sigma_x,\sigma_y)$, $0 \le \sigma_x < 1$, $\sigma_y \in \mathbb{R}$. Since the spectrum of $\hat{\mathcal{L}}(k_x;\sigma_x,\sigma_y)$ consists of isolated, real eigenvalues of finite multiplicity, one can use regular perturbation theory to calculate expansions of eigenvalues near $\mu = \sigma_x = \sigma_y = 0$. One finds that the spectrum is stable with the possible exception of a branch of eigenvalues

$$\lambda(\sigma_x,\sigma_y;k_x) = -d_\parallel(k_x)\sigma_x^2 - d_\perp(k_x)\sigma_y^2 + \mathrm{O}(4),$$

where $\mathrm{O}(4)$ refers to terms of order four, $\mathrm{O}(4)/(\sigma_x^4+\sigma_y^4) \le C$ for some $C < \infty$ as $\sigma_x, \sigma_y \to 0$.

In particular, the spectrum is stable, $\mathrm{Re}\,\lambda \le 0$, when effective diffusivities are positive $d_\parallel, d_\perp > 0$, a region in (k_x,μ)-space often referred to as the Busse balloon. The boundaries of this region are, for small μ, given by the Eckhaus boundary $k_\mathrm{eck}(\mu)$ and the zigzag boundary $k_\mathrm{zz}(\mu)$, where $d_\parallel$ is negative for $k_x > k_\mathrm{eck}$ and $d_\perp$ is negative for $k_x < k_\mathrm{zz}$. It turns out that stripes with $k = k_\mathrm{zz}$ possess minimal energy density and are therefore often preferred.

Our focus here will be on systems $(x,y) \in \mathbb{R} \times (\mathbb{R}/(L_y\mathbb{Z}))$ where the lateral period L_y is close to the critical zigzag period $L_y \sim 2\pi/k_\mathrm{zz}$. Ignoring the parameter jump at $x = 0$, we see that stripes with $k_x = 0$, $k_y = 2\pi/L_y$ are stationary solutions in such a strip, stable only when

$k_y > k_{\mathrm{zz}}$. In fact, choosing the lateral period such that $k_y < k_{\mathrm{zz}}$, we can find rotated stripes $u_{\mathrm{p}}(\kappa_x x + \kappa_y y; \kappa)$ with $\kappa_y = k_y$ and $\kappa_x = \sqrt{k_{\mathrm{zz}}^2 - k_y^2}$, such that the wavelength of this rotated pattern is precisely k_{zz}, thus minimizing the energy. This instability mechanism, often referred to as the zigzag instability is at the origin of much of the phenomenology in this paper. We refer to [19] for a broader background and to [28] for technical details.

2.2. Amplitude and phase diffusion equations. Striped patterns near a given orientation can be described by amplitude equations. We scale $y = k_y \tilde{y}$, and find, dropping tildes

$$u_t = -(\partial_{xx} + k_y^2 \partial_{yy} + 1)^2 u + \mu u - u^3. \tag{2.2}$$

Substituting an Ansatz $u(t, x, y) = \mathrm{e}^{\mathrm{i}y} A(t, x) + \mathrm{c.c.}$, assuming that μ is small and t, x are slowly varying, and collecting leading orders in μ, gives the Newell-Whitehead-Segel amplitude equation

$$A_t = -(\partial_{xx} + 2\varepsilon - \varepsilon^2)^2 A + \mu A - 3A|A|^2, \qquad \text{where } \varepsilon = 1 - k_y. \tag{2.3}$$

Writing $A = R\mathrm{e}^{\mathrm{i}\Phi}$, separating equations for R and Φ, and relaxing to $R = \sqrt{\mu/3}$ at leading order in ε, we find after a short calculation the Cross-Newell phase-diffusion equation,

$$\Phi_t = -c_4 \Phi_{xxxx} - c_1 \varepsilon \Phi_{xx} + c_3 \Phi_x^2 \Phi_{xx}, \qquad c_4 = 1, c_1 = 4, c_3 = 6; \tag{2.4}$$

see [19, §8.3] for the general strategy and [8, 44] for approximation results and limits of validity. Note that the coefficients in (2.4) are obtained from (2.3), thus leading-order in μ, only. One can more generally derive (2.4) directly from the Swift-Hohenberg equation near the zigzag instability, not necessarily at small μ. We computed coefficients $c_{1,3,4}$ numerically in this way, thus not using an asymptotic expression in μ, from the expansion of the dispersion relation, with deviations from (2.4) of order 10^{-4} for $\mu = 0.25$.

2.3. Spatial dynamics, knees, and more. A different approach [17] focuses on stationary patterns or traveling waves of (2.2) that remain close to horizontal striped patterns at all locations $x \in \mathbb{R}$, $u = u_{\mathrm{p}}(k_{\mathrm{zz}} y - \phi(x); k_{\mathrm{zz}} + w(x, y))$ in

$$-c_x u_x - c_y u_y = -(\partial_{xx} + k_y^2 \partial_{yy} + 1)^2 u + \mu u - u^3, \qquad u(x, y) = u(x, y + 2\pi), \tag{2.5}$$

with $k_y = k_{\mathrm{zz}} + \varepsilon$. One casts (2.5) as a first-order differential equation in x, requiring that w be orthogonal to u_{p}' and studies the resulting equations for ϕ and w from a dynamical systems point of view. One finds a family of equilibria, that is, x-independent solutions, $w \equiv 0$, $\phi \equiv \mathit{const}$, at $\varepsilon = 0$. Linearizing at these equilibria gives a length-4 Jordan block at the origin, with the rest of the spectrum being bounded away form the origin. A center-manifold reduction can thus be carried out, and one finds a fourth-order differential equation for ϕ, given at leading order through

$$\begin{aligned}
\phi_x &= \psi, \\
\psi_x &= v \\
v_x &= -4\varepsilon\psi + 2\psi^3 + m \\
m_x &= c_x \psi + c_y,
\end{aligned} \tag{2.6}$$

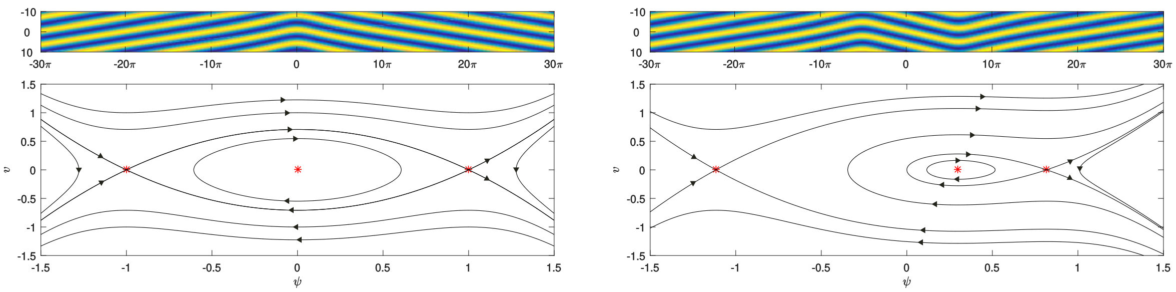

Figure 5. *Picture of knee solution (heteroclinic) and zigzag (homoclinic) in Swift-Hohenberg (top); phase portraits with corresponding heteroclinic and homoclinic orbits (bottom).*

where $\varepsilon = k_y - k_{\mathrm{zz}}$. Scaling

$$\psi = (2\varepsilon)^{1/2}\tilde{\psi},\ v = \sqrt{8}\varepsilon\tilde{v},\ m = \sqrt{32}\varepsilon^{3/2}\tilde{m},\ \partial_x = 2\varepsilon^{1/2}\partial_{\tilde{x}},\ c_x = 8\varepsilon^{3/2}\tilde{c}_x,\ c_y = 128\sqrt{\varepsilon}^2\tilde{c}_y, \tag{2.7}$$

eliminates ε-dependence and gives the the traveling-wave equation corresponding to the Cross-Newell equation (2.4), substituting an ansatz $\Phi = \phi(x - c_x t, t) - c_y t$.

In the specific case of the Swift-Hohenberg equation, the stationary equations (2.5) for $c_x = c_y = 0$ possess a Hamiltonian structure. Indeed, the system can be obtained as Euler-Lagrange equation to a variational problem with translation-invariance in x. Interpreting the energy as an action functional and the energy density as the Lagrangian, one then finds the Hamiltonian structure. In more detail, the energy interpreted as action functional is

$$\mathcal{E}[u] = \int_{x,y} \left(\frac{1}{2}\left(\partial_{xx}u + k_y^2\partial_{yy}u + u\right)^2 - \frac{1}{2}\varepsilon^2 u^2 + \frac{1}{4}u^4\right) \mathrm{d}x\mathrm{d}y.$$

We write (2.5) as a first order equation for $\underline{u} = (u, u_1, v, v_1)^T$ in the form

$$\begin{aligned} u_x &= u_1 \\ u_{1,x} &= v - k_y^2\partial_{yy}u - u \\ v_x &= v_1 \\ v_{1,x} &= -k_y^2\partial_{yy}v - v + \mu u - u^3, \end{aligned} \tag{2.8}$$

and define the Hamiltonian as

$$\mathcal{H}[\underline{u}] = \int_y h(\underline{u})\mathrm{d}y, \quad h(\underline{u}) = -\frac{1}{2}v^2 + u_1 v_1 + v(k_y^2 u_{yy} + u) - \frac{1}{2}u^2 + \frac{1}{4}u^4,$$

and the symplectic structure through [24]

$$\omega(\underline{u}, \underline{\tilde{u}}) = \int_y \underline{u} \cdot (\mathcal{J}\underline{\tilde{u}})\mathrm{d}y, \qquad \mathcal{J} = \begin{pmatrix} 0 & 0 & 0 & 1 \\ 0 & 0 & -1 & 0 \\ 0 & 1 & 0 & 0 \\ -1 & 0 & 0 & 0 \end{pmatrix}. \tag{2.9}$$

The translation symmetry in y corresponds to the conserved quantity

$$\mathcal{S}[\underline{u}] = -\int_y s(\underline{u}), \quad s(\underline{u}) = u(v_1)_y + v(u_1)_y, \quad \mathcal{J}\nabla_{L^2}\mathcal{S}[\underline{u}] = \partial_y \underline{u},$$

which we shall refer to as the momentum.

The tangent space to the center manifold is spanned [17] by

$$e_1 = \begin{pmatrix} u_\mathrm{p}'(y) \\ 0 \\ -(1+k_y^2\partial_{yy}u_\mathrm{p}') \\ 0 \end{pmatrix}, \; e_2 = \begin{pmatrix} 0 \\ u_\mathrm{p}'(y) \\ 0 \\ (1+k_y^2\partial_{yy})(1+k_y^2\partial_{yy})u_\mathrm{p}' \end{pmatrix},$$
$$e_3 = \begin{pmatrix} -\frac{1}{2}v_2(y) \\ 0 \\ u_\mathrm{p}'(y) - \frac{1}{2}(1+k_y^2\partial_{yy})v_2(y) \\ 0 \end{pmatrix}, \; e_4 = \begin{pmatrix} 0 \\ -\frac{1}{2}v_2(y) \\ 0 \\ u_\mathrm{p}'(y) - \frac{1}{2}(1+k_y^2\partial_{yy})v_2(y) \end{pmatrix}.$$

Here, $v_2(y)$ is the second derivative of the eigenvector for the Floquet-Bloch operator (2.1) in σ_y at $\sigma_x = 0$ [17]. One readily finds that the reduced flow (2.6) is obtained in this basis through $\underline{u}_\mathrm{c} = \phi e_1 + \psi e_2 + v e_3 + m e_4$. The symplectic structure, reduced Hamiltonian, and reduced momentum are, at leading order, in coordinates $U = (\phi, \psi, v, m)^T$, with $\mathcal{J}$ from (2.9),

$$\omega(U, \tilde{U}) = U \cdot (\mathcal{J}\tilde{U}), \quad H(U) = m\psi - \frac{1}{2}v^2 - 2\varepsilon^2\psi^2 + \frac{1}{2}\psi^4, \quad S(U) = m.$$

We note that heteroclinic orbits connect periodic orbits that are marginally stable with respect to the zigzag instability [24], due to conservation of $\mathcal{S}$. This follows from the fact that x-reflection changes the sign of $\mathcal{S}$ on a periodic pattern such that for heteroclinic orbits between reflected patterns necessarily $\mathcal{S} = 0$, which in turn holds precisely at the zigzag-critical stripes. On the other hand, one easily verifies that $\mathcal{S}$ is also conserved for a spatially inhomogeneous $\rho = \rho(x)$ that does not break the associated translation symmetry in y. As a consequence, since $\mathcal{S} = 0$ at $x = +\infty$ where $U \to 0$, the quenched system with $c_x = 0$ allows for oblique stripes at $x = -\infty$ only when $k = k_\mathrm{zz}$.

2.4. Spatial dynamics and effective boundary conditions. We consider (2.8) now with a parameter step, replacing the constant coefficient μ with $\rho = -\mu\,\mathrm{sign}(x)$. The considerations in the previous section provide a local description of solutions in a vicinity of the primary periodic stripe, for $x < 0$, only. The picture can be complemented by a description of dynamics in $x > 0$, where the origin $u = 0$ is a hyperbolic equilibrium. The following discussion is kept at a somewhat informal level as it is merely meant to motivate effective boundary conditions.

We first define the stable manifold W_+^s in $x > 0$ where $\rho = -\mu < 0$, as the set of initial conditions $(u, u_x, u_{xx}, u_{xxx})(y)$ at $x = 0$ that give rise to solutions converging to the origin as $x \to +\infty$. Next, we define the center-unstable manifold W_-^cu, in $x < 0$ where $\rho = \mu > 0$, as the set of initial conditions at $x = 0$ that give rise to solutions that converge to the center manifold W_-^c for the dynamics in $x < 0$ near the stripes, as $x \to -\infty$. Solutions of interest to us lie in the intersection of $W_+^\mathrm{s} \cap W_-^\mathrm{cu}$.

Fredholm theory shows that a transverse intersection of these two manifolds would consist of a two-dimensional submanifold of W^{cu}_{-}. Since W^{cu}_{-} is foliated over the 4-dimensional center manifold W^{c}, we may assume that the submanifold is transverse to this foliation and then project this two-dimensional submanifold along the smooth foliation onto the center manifold W^{c}, where it gives rise to a two-dimensional submanifold $\mathcal{B}$ of W^{c}. By construction, initial conditions on this two-dimensional submanifold that give rise to bounded solutions on the center manifold as $x \to -\infty$ correspond to bounded solutions on $x \in \mathbb{R}$, after lifting to the corresponding intersection point in the unstable foliation.

The construction outlined above yields, under some transversality assumptions, the existence of *effective boundary conditions*, a two-dimensional submanifold $\mathcal{B} \subset W^{\mathrm{c}}$. By translation invariance with respect to the shift in y, the center manifold W^{c}, the local flow on W^{c}, and the effective boundary condition $\mathcal{B}$ are invariant under this translation, which is simply given through the additive action $\phi \mapsto \phi + \varphi$ on the circle. As a consequence, $\mathcal{B} = \{(\psi, v, m) \in B\}$ for some one-dimensional manifold B which we parameterize as $(\psi_B(\sigma), v_B(\sigma), m_B(\sigma))$, $\sigma \sim 0$, with $\psi_B(0) = v_B(0) = m_B(0) = 0$.

Within the center-manifold, the scaling $\tilde{x} = \sqrt{\varepsilon}x$, $\tilde{\psi} = \sqrt{\varepsilon}\psi$, $\tilde{v} = \varepsilon v$, $\tilde{m} = \varepsilon^{3/2}m$ that reduces to the ε-independent Cahn-Hilliard equation (2.7), eliminates the parameter ε at leading order and gives the Cahn-Hilliard steady-state equation. With this scaling, the boundary curve $\mathcal{B}$ is transformed to $B_\varepsilon \sim (0, 0, \sigma)$ provided that $m'_B(0) \neq 0$. In this sense, we expect a typical clamped boundary condition

$$\psi = \psi_x = 0 \text{ at } x = 0. \tag{2.10}$$

Of course, these boundary conditions would be accurate only at leading order in ε.

In the specific case of the Swift-Hohenberg equation with a parameter step, the boundary manifold is not "generic" in the sense that the tangent space at the origin is given by $\psi = \psi_{xx} = 0$. This non-genericity is caused by the Hamiltonian structure of the reduced equation, or, more specifically, by the conservation of momentum. In fact, the equation with parameter jump in x possesses the y-translation symmetry such that the momentum S is conserved in x. Therefore, S evaluated on the effective boundary conditions coincides with S evaluated at the origin, $x = +\infty$. As a consequence, the boundary manifold B_ε is contained in $\{m = 0\}$. A generic curve through the origin in the (ψ, v)-plane will, after scaling, reduce to the line $\psi = 0$, which together with $m = 0$ gives the Dirichlet boundary conditions

$$\psi = \psi_{xx} = 0 \text{ at } x = 0. \tag{2.11}$$

We would expect small non-variational effects to yield boundary conditions that interpolate between Dirichlet and clamped, and therefore also study a straight interpolation,

$$\psi = \tau\psi_x + (1 - \tau)\psi_{xx} = 0. \text{ at } x = 0, \tag{2.12}$$

for $0 \leq \tau \leq 1$. Finally, we shall also consider the time-dependent, scaled version,

$$\psi_t = -(\psi_{xx} + \psi - \psi^3)_{xx} + c_x\psi_x, \tag{2.13}$$

obtained from (2.4) by scaling and setting $\psi = \Phi_x$, together with the boundary conditions (2.10) and (2.11). We emphasize that for any of the choices of boundary conditions, mass $\int \psi$ is not conserved at the boundary. In particular, solutions with $\psi = 0$ at the boundary and $\psi \to \eta \neq 0$ for $x \to -\infty$ are possible.

3. Slow growth: A singular heteroclinic perturbation problem. We analyze the stationary equation $c_x = 0$ (2.6) in §3.1 and set up a perturbation analysis with $c_x \gtrsim 0$ in §3.2. We relegate some more technical aspects of the analysis to §3.3 which the reader may skip at first reading. The results in this section establish existence in the lower light gray region of Fig. 4, left panel.

3.1. Oblique stripes at zero speed. We study (2.6) in the scaling (2.7), and omit the trivial equation for ϕ,

$$\begin{aligned} \psi_x &= v \\ v_x &= -\psi + \psi^3 + m \\ m_x &= c_x\psi + c_y. \end{aligned} \tag{3.1}$$

First, set $c_x = c_y = 0$ which gives $m \equiv const$ and a remaining family of nonlinear pendulum equation; see Fig. 6. Clamped boundary conditions correspond to a shooting problem from the line $\psi = v = 0$ to backward spatial time $x < 0$. Dirichlet boundary conditions correspond to a similar shooting problem, now from the line $\psi = m = 0$. We readily find the solution

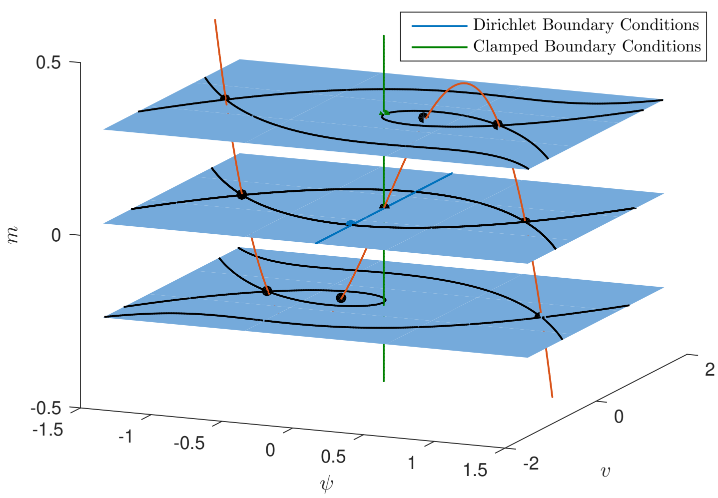

Figure 6. *Phase portrait for (3.1) at $c_x = c_y = 0$, including straight lines defined by boundary conditions at $x = 0$ and the heteroclinic and homoclinic intersections with the boundary conditions.*

$\psi_\mathrm{d}(x) = \pm\tanh(x/\sqrt{2})$ for Dirichlet boundary conditions, simply "half" of a knee solution described in the previous section (see Fig. 5, left panel). For clamped boundary conditions, we find $\psi_\mathrm{cl}(x) \to \eta_*$ for $x \to -\infty$, simply "half " of the step solution described above, with "explicit" expression,

$$\psi'_\mathrm{cl} = (\psi_\mathrm{cl} - \eta_*)\sqrt{\frac{1}{2}\psi_\mathrm{cl}(\psi_\mathrm{cl} + 2\eta_*)}, \qquad m_* = \eta_* - \eta_*^3,\ \eta_* = \sqrt{2/3}; \tag{3.2}$$

see Fig. 5. Conservation of m leads to degenerate dynamics in $\mathbb{R}^3$ with families of equilibria. Perturbations with c_x and c_y that break this degeneracy should be viewed as singular perturbations in the sense of [9]. While one could go ahead and study this singular perturbation problem geometrically following the ideas there, we choose a somewhat more direct and possibly more self-contained approach using farfield-core decompositions.

3.2. Oblique stripes for $c_x \gtrsim 0$.

Our main analytical result is as follows.

Theorem 3.1. *Consider (3.1) with either clamped (2.10) or Dirichlet (2.11) boundary conditions, near the profiles $\psi_{\mathrm{cl/d}}$ and near $c_x = c_y = 0$. For all c_x sufficiently small, there exists a smooth function $c_y = -c_x \cdot \eta_{\mathrm{cl/d}}(c_x)$ and solutions $\psi_{\mathrm{cl/d}}(x; c_x)$ such that $\psi_{\mathrm{cl/d}}(x; c_x) \to \eta_{\mathrm{cl/d}}(c_x)$ for $x \to -\infty$ and $\psi_{\mathrm{cl/d}}$ satisfy (2.10) or (2.11), respectively. Moreover, $\psi_{\mathrm{cl/d}}$ and its derivatives depend smoothly on c_x as smooth functions, locally uniformly. We have the expansions*

(3.3)
$$\eta_{\mathrm{cl}}(c_x) = \sqrt{\frac{2}{3}} - \left(\sqrt{6} - \sqrt{2}\log(2+\sqrt{3})\right) c_x + \mathrm{O}(c_x^2) \qquad \eta_{\mathrm{d}}(c_x) = 1 - \frac{\sqrt{2}\log(2)}{2} c_x + \mathrm{O}(c_x^2).$$

We prove Theorem 3.1 in the remainder of this section, up to some more technical aspects that we treat with more care in the next section. The key initial step is to decompose the solution into a constant piece near infinity plus an exponentially localized perturbation. Specifically, we introduce a smooth cutoff function $0 \le \chi_- \le 1$, $\chi_- \equiv 1$ for $x < -2$, $\chi_- \equiv 0$ for $x > -1$, and look for solutions of the form

$$\begin{pmatrix} \psi \\ v \\ m \end{pmatrix} = \begin{pmatrix} \hat{\psi} + \chi_- \eta \\ v \\ \hat{m} + \chi_-(\eta - \eta^3) \end{pmatrix}, \tag{3.4}$$

where η is a constant to be determined, and $\hat{\psi}$, v, and $\hat{m}$ decay exponentially at $-\infty$. We then write (3.1), with $c_y = -c_x\eta$, as an equation for $\hat{\psi}, v, \hat{m}$ and η in the form

$$F(\hat{\psi}, v, \hat{m}, \eta; c_x) := \begin{pmatrix} \hat{\psi}' + \chi_-'\eta - v \\ v' + \hat{\psi} - \hat{m} - \hat{\psi}^3 - 3\hat{\psi}^2\chi_-\eta - 3\hat{\psi}(\chi_-\eta)^2 + (\chi_- - \chi_-^3)\eta^3 \\ \hat{m}' - c_x\hat{\psi} + \chi_-'(\eta - \eta^3) + c_x(1-\chi_-)\eta \end{pmatrix} = 0, \tag{3.5}$$

in an appropriately chosen exponentially weighted function space. The choice (3.4) implies that (3.5) has an explicit solution at $c_x = 0$ given by

$$\begin{aligned} \eta_0 &= \eta_*^{\mathrm{cl/d}}, \\ \hat{\psi}_0 &= \psi_{\mathrm{cl/d}} - \chi_-\eta_*^{\mathrm{cl/d}}, \\ v_0 &= \psi_{\mathrm{cl/d}}', \\ \hat{m}_0 &= (1-\chi_-)\left(\eta_*^{\mathrm{cl/d}} - (\eta_*^{\mathrm{cl/d}})^3\right), \end{aligned} \tag{3.6}$$

where $\eta_*^{\mathrm{cl}} = \sqrt{2/3}$ and $\eta_*^{\mathrm{d}} = 1$ are the limits of $\psi_{\mathrm{cl/d}}$ at $-\infty$. For ease of notation, let $u_0^{\mathrm{cl/d}} = (\hat{\psi}_0, v_0, \hat{m}_0, \eta_0; 0)$ denote this trivial solution. We will drop the sub- and super-scripts “cl/d” when the difference is irrelevant.

In the following section, we use Fredholm properties to prove that the linearization of F at the trivial solution is invertible in appropriately chosen spaces. The implicit function theorem then guarantees the existence of unique solutions to (3.5) near this trivial solution as well as smooth dependence on c_x, proving the first part of Theorem 3.1. Uniqueness guarantees $\eta_{\mathrm{cl/d}}(0) = \eta_*^{\mathrm{cl/d}}$, giving the zeroth order terms in the asymptotics. In computing the coefficient at the next order, we make use of the following fact from linear theory in §3.3:
Fact: Let $\mathcal{L} = \partial_{\hat{\psi},v,\hat{m}} F(u_0)$ denote the linearization of F at its trivial solution with respect to its first three arguments, and let $\mathcal{L}^*$ be the adjoint of $\mathcal{L}$ with respect to the standard L^2 inner product. The kernel of $\mathcal{L}^*$ is one dimensional, spanned by $e_*^{\mathrm{cl}} = (-\psi_{\mathrm{cl}}'', \psi_{\mathrm{cl}}', -\psi_{\mathrm{cl}})$ for clamped boundary conditions and by $e_*^{\mathrm{d}} = (0, 0, 1)$ for Dirichlet boundary conditions.

Once we have existence of solutions and smooth dependence on parameters, differentiating (3.5) gives, via the chain rule,

$$\mathcal{L}\left(\partial_{c_x}(\hat{\psi}(c_x), v(c_x), \hat{m}(c_x))\big|_{c_x=0}\right) + \partial_\eta F(u_0)\eta'(0) + \partial_{c_x} F(u_0) = 0. \tag{3.7}$$

The first term may be eliminated by projecting onto the kernel of $\mathcal{L}^*$, which is orthogonal to the range of $\mathcal{L}$. We thereby find explicit expressions for $\eta'(0)$ in terms of projections onto the adjoint kernel:

$$\eta_{\mathrm{cl/d}}'(0) = -\frac{\langle \partial_{c_x} F(u_0^{\mathrm{cl/d}}), e_*^{\mathrm{cl/d}} \rangle}{\langle \partial_\eta F(u_0^{\mathrm{cl/d}}), e_*^{\mathrm{cl/d}} \rangle}. \tag{3.8}$$

These derivatives are given explicitly, after some simplification, by

$$\partial_\eta F(u_0) = \begin{pmatrix} \chi_-' \\ 3\chi_-\left((\eta_*^{\mathrm{cl/d}})^2 - (\psi_*^{\mathrm{cl/d}})^2\right) \\ \chi_-'(1 - 3(\eta_*^{\mathrm{cl/d}})^2) \end{pmatrix} \text{ and } \partial_{c_x} F(u_0) = \begin{pmatrix} 0 \\ 0 \\ \eta_*^{\mathrm{cl/d}} - \psi_{\mathrm{cl/d}} \end{pmatrix}. \tag{3.9}$$

For clamped boundary conditions, we find

$$\begin{aligned} \langle \partial_{c_x} F(u_0^{\mathrm{cl}}), e_*^{\mathrm{cl}} \rangle &= \int_{-\infty}^0 (\eta_*^{\mathrm{cl}} - \psi_{\mathrm{cl}})(-\psi_{\mathrm{cl}})\,\mathrm{d}x = \int_{\eta_*^{\mathrm{cl}}}^0 (\psi_{\mathrm{cl}} - \eta_*^{\mathrm{cl}})\psi_{\mathrm{cl}} \frac{d\psi_{\mathrm{cl}}}{\psi_{\mathrm{cl}}'} \\ &= \int_{\eta_*^{\mathrm{cl}}}^0 \frac{(\psi_{\mathrm{cl}} - \eta_*^{\mathrm{cl}})\psi_{\mathrm{cl}}}{(\psi_{\mathrm{cl}} - \eta_*^{\mathrm{cl}})\sqrt{\frac{1}{2}\psi_{\mathrm{cl}}(\psi_{\mathrm{cl}} + 2\eta_*^{\mathrm{cl}})}} d\psi_{\mathrm{cl}} = \int_{\eta_*^{\mathrm{cl}}}^0 \frac{\sqrt{2\psi_{\mathrm{cl}}}}{\sqrt{\psi_{\mathrm{cl}} + 2\eta_{\mathrm{cl}}}} d\psi_{\mathrm{cl}} \\ &= \frac{2\log(2+\sqrt{3})}{\sqrt{3}} - 2, \end{aligned} \tag{3.10}$$

where we have used (3.2) to write ψ_{cl}' in terms of ψ_{cl}. For the denominator, we find after integrating by parts,

$$
\begin{aligned}
\langle \partial_\eta F(u_0^{\mathrm{cl}}), e_*^{\mathrm{cl}}\rangle &= \int_{-\infty}^0 -\psi_{\mathrm{cl}}''\chi_-' + \psi_{\mathrm{cl}}'(3\chi_-((\eta_*^{\mathrm{cl}})^2 - \psi_{\mathrm{cl}}^2)) - \psi_{\mathrm{cl}}\chi_-'(1-3(\eta_*^{\mathrm{cl}})^2)\,\mathrm{d}x \\
&= \int_{-\infty}^0 (-\psi_{\mathrm{cl}}'' - \psi_{\mathrm{cl}}(1-3(\eta_*^{\mathrm{cl}})^2) - 3\psi_{\mathrm{cl}}(\eta_*^{\mathrm{cl}})^2 + \psi_{\mathrm{cl}}^3)\chi_-'\,\mathrm{d}x \\
&\qquad\qquad + \Big[(3\psi_{\mathrm{cl}}\chi_-(\eta_*^{\mathrm{cl}})^2) - \psi_{\mathrm{cl}}^3\chi_-\Big]_{-\infty}^0 \\
&= \int_{-\infty}^0 -m_*\chi_-'\,\mathrm{d}x + 3\psi_{\mathrm{cl}}(\eta_*^{\mathrm{cl}})^2 - \psi_{\mathrm{cl}}^3\big|_{-\infty} \\
&= m_* - 2\eta_*^3 = \eta_*^{\mathrm{cl}} - 3(\eta_*^{\mathrm{cl}})^3 = -\sqrt{\frac{2}{3}}. \qquad (3.11)
\end{aligned}
$$

Inserting (3.10) and (3.11) into (3.8) gives the leading coefficient in the asymptotics of Theorem 3.1 for clamped boundary conditions.

For Dirichlet boundary conditions, where $e_*^{\mathrm{d}} = (0,0,1)$, we instead find

$$
\langle \partial_{c_x} F(u_0^d), e_*^{\mathrm{d}}\rangle = \int_{-\infty}^0 \left(\eta_*^d - \psi_d\right)\,\mathrm{d}x = \int_{-\infty}^0 \left(1 + \tanh\left(x/\sqrt{2}\right)\right)\,\mathrm{d}x = \sqrt{2}\log(2)
$$

and

$$
\langle \partial_\eta F(u_0^d), e_*^{\mathrm{d}}\rangle = \int_{-\infty}^0 \chi_-'\left(1 - 3(\eta_*^d)^2\right)\,\mathrm{d}x = 3(\eta_*^d)^2 - 1 = 2,
$$

which yields the linear asymptotics for Dirichlet boundary conditions and completes the proof of Theorem 3.1, up to the technical aspects that we present in the next section.

3.3. Weighted spaces, Fredholm properties, and the implicit function theorem. We construct function spaces $X_{\mathrm{cl/d}}$ and view F as an operator $F : X_{\mathrm{cl/d}} \times \mathbb{R}^2 \to (L_\delta^2(\mathbb{R}^-))^3$, defined as follows. First, for $\delta > 0$ small, let $H_\delta^1(\mathbb{R}^-)$ denote the weighted Sobolev space of weakly differentiable functions on $x < 0$ with finite H_δ^1 norm, given by

$$
||f(x)||_{H_\delta^1}^2 = ||e^{-\delta x} f(x)||_{H^1}^2 \sim \int_{-\infty}^0 (|f(x)|^2 + |f'(x)|^2) e^{-2\delta x}\,\mathrm{d}x, \qquad (3.12)
$$

where $\sim$ denotes equivalence of these two norms. Then, we define

$$
X_{\mathrm{cl}} = \{(\hat\psi, v, \hat m) \in (H_\delta^1(\mathbb{R}^-))^3 : \hat\psi(0) = v(0) = 0\}, \qquad (3.13)
$$

and

$$
X_{\mathrm{d}} = \{(\hat\psi, v, \hat m) \in (H_\delta^1(\mathbb{R}^-))^3 : \hat\psi(0) = \hat m(0) = 0\} \qquad (3.14)
$$

as the subspaces of $(H_\delta^1(\mathbb{R}^-))^3$ satisfying clamped and Dirichlet boundary conditions, respectively. That F is a well-defined and differentiable function between these spaces follows from the fact that $H^1_\delta(\mathbb{R}^-)$ is a Banach algebra, a property inherited from $H^1(\mathbb{R}^-)$ in combination with the fact that multiplication by $e^{\delta x}$ is a bounded operator on $H^1(\mathbb{R}^-)$ for $\delta > 0$, so

$$||fg||_{H^1_\delta} = ||e^{-\delta x} f(x)g(x)||_{H^1} \le C||e^{-\delta x} f(x) e^{-\delta x} g(x)||_{H^1} \le C||f||_{H^1_\delta}||g||_{H^1_\delta}.$$

The linear operator $\mathcal{L} : X_{\mathrm{cl/d}} \to (L^2_\delta(\mathbb{R}^-))^3$ defined in the previous section is the Fréchet derivative of F evaluated at the trivial solution defined in (3.6), and is given explicitly by,

$$\mathcal{L}\begin{pmatrix}\hat\psi_1\\ v_1\\ \hat m_1\end{pmatrix} = \begin{pmatrix}\hat\psi_1' - v_1\\ v_1' + (1-3\psi^2_{\mathrm{cl/d}})\hat\psi_1 - \hat m_1\\ \hat m_1',\end{pmatrix}. \tag{3.15}$$

The key ingredients now are Fredholm properties of $\mathcal{L}$, which determine our choice of δ.

Lemma 3.2 (Fredholm properties). *For $\delta > 0$ sufficiently small, $\mathcal{L}$ is a Fredholm operator with index -1, trivial kernel, and one dimensional cokernel.*

Proof. If $(\hat\psi_1, v_1, \hat m_1) \in \ker(\mathcal{L})$, the third equation implies $\hat m_1$ is constant, hence vanishes since our weights enforce localization. The first two equations then reduce to

$$\hat\psi_1'' + (1-3\psi^2_{\mathrm{cl/d}})\hat\psi_1 = 0, \tag{3.16}$$

which is simply the linearization of the pendulum equation for $\psi_{cl/d}$. Translation invariance of this differential equation guarantees that $\hat\psi_1 = \psi'_{\mathrm{cl/d}}$ is a solution to (3.16). Since the Wronskian is constant, a second, linearly independent solution to (3.16) necessarily grows exponentially and we conclude that $\psi_{\mathrm{cl/d}}$ is the unique solution that is bounded at $x = -\infty$. Hence, for $\delta > 0$, $\hat\psi_1 = \psi'_{\mathrm{cl/d}}$ is the only solution to (3.16) that is contained in our weighted space. In the case of clamped boundary conditions $\hat\psi_1'(0) = \psi''_{\mathrm{cl}}(0) \neq 0$, so the solution does not satisfy the boundary conditions at $x = 0$. For Dirichlet boundary conditions, $\hat\psi(0) = \psi'_d(0) \neq 0$, and again the boundary conditions are not satisfied. Thus, the kernel of $\mathcal{L}$ is trivial.

We find the cokernel by viewing $\mathcal{L}$ as a closed, densely defined operator on $(L^2(\mathbb{R}^-))^3$ and computing its adjoint $\mathcal{L}^*$ with respect to the standard L^2 inner product. The boundary conditions for the adjoint are the orthogonal complement to the boundary conditions for $\mathcal{L}$, i.e. the domain of $\mathcal{L}^*$ is the dense subspace of $(L^2(\mathbb{R}^-))^3$ defined by

$$Y_{\mathrm{cl}} = \{(\hat\psi_1, v_1, \hat m_1) \in (H^1_{-\delta}(\mathbb{R}^-))^3 : \hat m_1(0) = 0\} \tag{3.17}$$

in the clamped case and

$$Y_{\mathrm{d}} = \{(\hat\psi_1, v_1, \hat m_1) \in (H^1_{-\delta}(\mathbb{R}^-))^3 : v_1(0) = 0\} \tag{3.18}$$

in the Dirichlet case. In both cases, $\mathcal{L}^*$ is defined by the formula

$$\mathcal{L}^*\begin{pmatrix}\hat\psi_1\\ v_1\\ \hat m_1\end{pmatrix} = \left[-\frac{\mathrm{d}}{\mathrm{d}x} + \begin{pmatrix}0 & 1-3\psi^2_{\mathrm{cl/d}} & 0\\ -1 & 0 & 0\\ 0 & -1 & 0\end{pmatrix}\right]\begin{pmatrix}\hat\psi_1\\ v_1\\ \hat m_1\end{pmatrix} = \begin{pmatrix}-\hat\psi_1' + (1-3\psi^2_{\mathrm{cl/d}})v_1\\ -v_1' - \hat\psi_1\\ -\hat m_1' - v_1\end{pmatrix}. \tag{3.19}$$

Searching for the kernel of $\mathcal{L}^*$ reduces to solving

$$\begin{aligned} v_1'' + (1 - 3\psi_{\mathrm{cl/d}}^2)v_1 &= 0, \\ \hat{\psi}_1 &= -v_1', \\ \hat{m}_1' &= -v_1 \end{aligned} \tag{3.20}$$

with appropriate boundary conditions given by (3.17) and (3.18), respectively. The equation for v_1 is again the linearization of the equation for $\psi_{\mathrm{cl/d}}$, hence we obtain solutions

$$(\hat{\psi}_1, v_1, \hat{m}_1) = (-\alpha\psi_{\mathrm{cl/d}}'', \alpha\psi_{\mathrm{cl/d}}', -\alpha\psi_{\mathrm{cl/d}} + \beta),$$

for arbitrary constants α and β. Choosing δ sufficiently small guarantees that these are the only possible solutions, as the other linearly independent solution of the equation for v_1 must grow exponentially with some fixed rate, since the Wronskian is constant. For clamped boundary conditions (3.17), we obtain $\beta = 0$, hence the cokernel is spanned by $e_*^{\mathrm{cl}} = (-\psi_{\mathrm{cl}}'', \psi_{\mathrm{cl}}', -\psi_{\mathrm{cl}})$. Dirichlet boundary conditions (3.18) force $\alpha = 0$, since $\psi_d'(0) \neq 0$, so in this case the cokernel is spanned by $e_*^{\mathrm{d}} = (0, 0, 1)$. Note that constants and asymptotically constant functions are allowed in our space due to the exponential weight, now appearing with opposite sign $-\delta$ for the L^2-dual of L^2_δ. In either case, the cokernel is one dimensional, as claimed.

To complete the proof, one needs to verify that $\mathcal{L}$ has closed range. To see this, note that the operator $\rho : (\hat{\psi}_1(x), v_1(x), \hat{m}_1(x)) \mapsto (e^{-\delta x}\hat{\psi}_1(x), e^{-\delta x}v_1(x), e^{-\delta x}\hat{m}_1(x))$ is an isometric isomorphism from $(L^2_\delta(\mathbb{R}^-))^3 \to (L^2(\mathbb{R}^-))^3$. The conjugate operator $\mathcal{L}_\rho := \rho \circ \mathcal{L} \circ \rho^{-1}$ (fixing η and c_x and viewing $\mathcal{L}$ as a function of its first three arguments only) is then of the form $\partial_x + A(x)$, where $x \mapsto A(x)$ is a continuous mapping with limit $A_- := \lim_{x\to-\infty} A(x)$ a hyperbolic matrix. The proof that the range of $\mathcal{L}$ is closed then follows by applying the argument of [35, Theorem 2.1], to $\mathcal{L}_\rho$ and making use of this isomorphism. ∎

In order to solve (3.5) using the implicit function theorem, we make use of our farfield-core decomposition to treat η as a variable. Provided the linearization $\partial_\eta F(u_0^{\mathrm{cl/d}})$ does not lie in the range of $\mathcal{L}$, appending η as a variable increases the dimension of the range of the derivative of F by 1, and hence the derivative becomes invertible. The implicit function theorem then gives the existence of a unique solution $(\hat{\psi}(c_x), v(c_x), \hat{m}(c_x), \eta(c_x); c_x)$ near u_0 in $X_{\mathrm{cl/d}} \times \mathbb{R}^2$ (in particular for sufficiently small c_x), depending smoothly on c_x. Thus, the argument is complete once we prove the following lemma:

Lemma 3.3 (Transversality). *The derivative $\partial_\eta F(u_0^{\mathrm{cl/d}})$ does not lie in the range of $\mathcal{L}$.*

Proof. The range of $\mathcal{L}$ is orthogonal to the kernel of $\mathcal{L}^*$. In §3.2, we computed the projections of $\partial_\eta F(u_0^{\mathrm{cl/d}})$ onto the respective adjoint kernels, and found them to be nonzero, which proves the lemma. ∎

Remark 3.4 (Geometry). The fact that $\partial_\eta F(u_0^{\mathrm{cl/d}})$ does not lie in the range, or, equivalently, that the scalar product with the kernel of the adjoint does not vanish, has an equivalent geometric interpretation in terms of transversality, hence the name of Lemma 3.3. In the Dirichlet case, both unstable manifold $\eta = 1$ and the subspace of solutions satisfying the boundary conditions are one-dimensional. Adding η as a parameter, we merely consider the center-unstable manifold, now two-dimensional, and show that it intersects the boundary subspace transversely, which in turn is seen inspecting the phase portrait.

4. Moderate growth rates: from oblique stripes to zigzags through homoclinic bifurcations.

We analyze the Cahn-Hilliard approximation (2.13) for moderate speeds $c_x > 0$ with clamped or Dirichlet boundary conditions at $x = 0$. We investigate existence of heteroclinic orbits using numerical continuation, finding a solution set that we refer to as the kink-dragging bubble in §4.1. We then analyze the endpoint of maximal c_x where a saddle-node bifurcation gives rise to time-periodic solutions, §4.2, which in turn disappear in a detachment process for yet larger speeds, §4.3. The analysis here completes the picture within the Cahn-Hilliard approximation schematically represented in the left panel of Fig. 4.

4.1. The kink-dragging bubble.

Having established existence of oblique stripe formation for small c_x in the previous section, we pursue moderate values of c_x using heteroclinic continuation. The results here extend the light gray existence region in the left panel of Fig. 4 to the dark region and discuss in particular the upper boundary of dark gray existence.

We solve (3.1) numerically setting $c_y = -\eta c_x$,

$$\begin{cases} \psi_x = v \\ v_x = -\psi + \psi^3 + m \quad \text{in } -L < x < 0, \\ m_x = c_x(\psi - \eta) \end{cases} \qquad \begin{cases} \psi = 0, \quad \tau v + (1-\tau)m = 0, & \text{at } x = 0, \\ \psi = \eta, \quad v = 0, & \text{at } x = -L, \end{cases}$$

The parameter τ interpolates between Dirichlet boundary conditions $\psi = \psi_{xx} = 0$ at $\tau = 0$ and clamped boundary conditions $\psi = \psi_x = 0$ at $\tau = 1$.

Note that the three-dimensional ODE is equipped with 4 boundary conditions. The resulting overdetermined system is solved by leaving the asymptotic angle η as a free variable, a procedure which mimics well the Fredholm analysis in §3.1. The number of boundary conditions at $x = -L$ can also be understood as defining a one-dimensional linear subspace which approximates the one-dimensional unstable manifold of the equilibrium $\psi = \eta$ at zeroth order. We used arc-length continuation with parameter c_x starting at $c_x = 0$; see Fig. 7

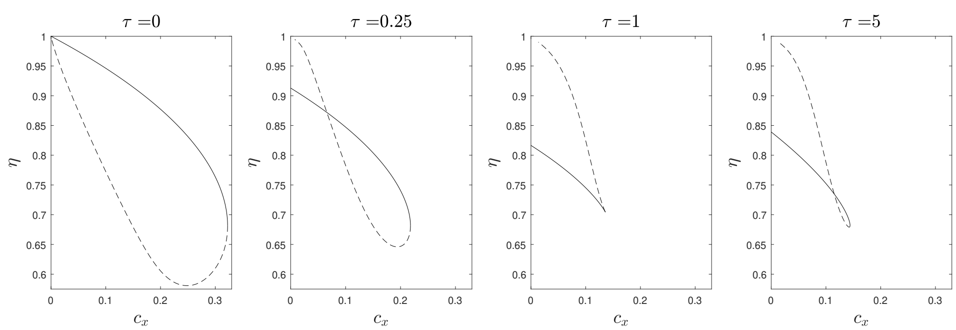

Figure 7. *Bifurcation diagrams of heteroclinic orbits in (4.1) for several values of the boundary homotopy parameter τ, plotting $\eta = \psi(x = -L)$ (orientation of oblique stripes) as a function of speed c_x; solid lines correspond to linearly stable, dashed to unstable solutions.*

for results. The saddle-node bifurcation occurs at $c_x^{\text{osn}} = 0.136$, $\eta^{\text{osn}} = 0.704$ for clamped boundary conditions and $c_x^{\text{osn}} = 0.322$, $\eta^{\text{osn}} = 0.681$ for Dirichlet boundary conditions. Note that the saddle-node is apparently degenerate in the projection onto η in the case of clamped boundary conditions, a fact that we corroborated by computing the kernel at the saddle-node location which exhibits a zero η-component. We illustrate how the "folding" at the saddle-node changes orientation near $\tau = 1$ by continuing the homotopy past $\tau = 1$. Incidentally, we found that c_x^{osn} is minimal at $\tau = 1$.

Fig. 8 shows selected solutions profiles and spectra of linearized operators obtained from linearizing (2.13) at these stationary solutions. We notice that, continuing through the saddle-node, solution profiles turn non-monotone at the bifurcation point and, continuing back to $c_x = 0$ on the unstable branch, ultimately develop a kink. In an unbounded domain, solutions on the unstable branch converge locally uniformly as $c_x \searrow 0$ to the reflected solution with $\eta = -\eta(c_x = 0)$, while a kink near $x = -\infty$ mediates a jump back from $\eta = -1$ to $\eta = +1$.

The linearized spectra, computed in large domains, approximate the extended point spectrum and the absolute spectrum in the unbounded domain; see [36]. We computed the curves given by the absolute spectrum of $-\partial_x^4 + (1 - 3\eta^2)\partial_x^2 + c_x\partial_x$ via continuation as outlined in [34]. We confirmed that most eigenvalues cluster on these curves, with the exception of a simple isolated real eigenvalue that crosses the origin in the saddle-node bifurcation.

The rightmost points of the absolute spectrum are pinched double roots which are stable as long as the selected state $\eta(c_x^{\mathrm{osn}})$ is convectively stable (which is true for all computed profiles, here since $\eta > 1/\sqrt{3}$ is linearly stable). Note that the spectrum in the unbounded domain contains a branch of continuous spectra, inherited from the linearization at $\psi \equiv \eta$, that can be readily computed using the Fourier transform as

$$\lambda = -k^4 + (1 - 3\eta^2)k^2 + c_x\mathrm{i}k, \qquad k \in \mathbb{R}.$$

The zero mode $\lambda = k = 0$ is caused by neutral mass conservation at $x = -\infty$.

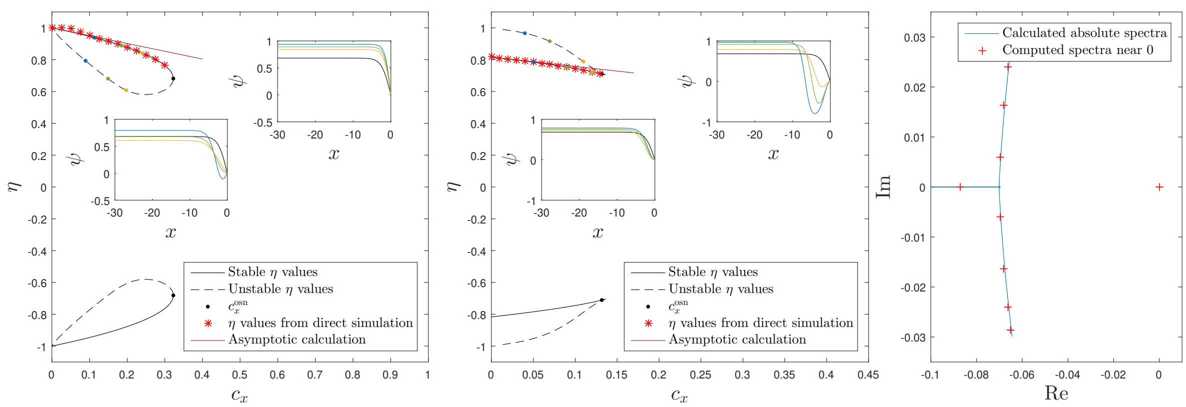

Figure 8. *Bifurcation diagrams for (4.1), $\tau = 0$ (left) and $\tau = 1$ (center), with computed profiles in insets and red markers for values from direct simulations. The right figure shows the spectrum of the linearization at the critical equilibrium, demonstrating that the saddle-node bifurcation is caused by an isolated eigenvalue. Blue superimposed lines show absolute spectra; see text for details.*

In order to further demonstrate the nature of the saddle-node bifurcation, we investigated perturbations of the unstable equilibrium close to the saddle-node in direct simulations. We found the typical separation of the neighborhood of the unstable equilibrium by a codimension-one stable manifold. Perturbations on either side of this manifold lead to either release of a single kink and convergence to the reflected, negative, stable equilibrium, or to convergence to the stable equilibrium nearby after annihilation of the trapped kink in the unstable profile at the boundary $x = 0$, respectively; see Figure 9.

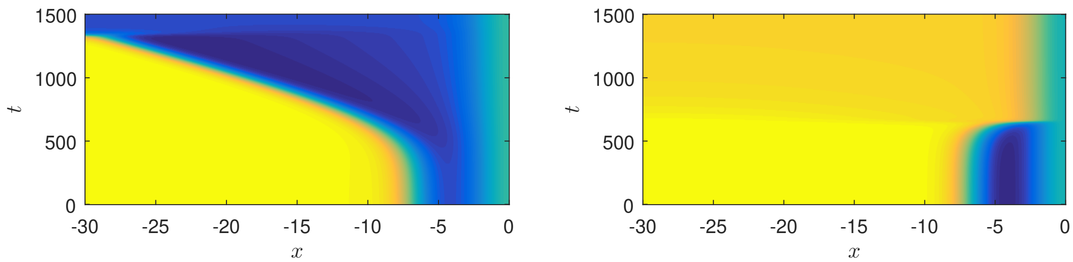

Figure 9. *Space-time plots of perturbations of the unstable solution profile, resulting in either release (left) or annihilation (right) of the kink; see text for details.*

4.2. Kink-shedding — saddle-node on a limit cycle. This section is concerned with zigzagging past the saddle-node, near the lower boundary of the orange region in the left panel of Fig. 4. The simulations in Fig. 9 suggest that heteroclinic orbits connect the two saddle-node equilibria conjugate by reflection $\psi \to -\psi$, in a locally uniform sense, thus forming a (double, since there are two equilibria) saddle-node bifurcation on a limit cycle. One therefore expects to observe, for parameter values c_x just past the saddle-node, a periodic orbit with large temporal period, due to slow passages near the region in phase space where the saddle-node was located. This periodic orbit corresponds to periodically changing the sign of ψ, which in turn yields a zigzag or wrinkled pattern in the original Swift-Hohenberg equation. One can therefore infer leading-order asymptotics of the period of the periodic orbit from the leading-order expansion of dynamics on the center-manifold, only. We shall compare such predictions with periods measured in direct simulations, here.

Before calculating this expansion, we notice however a technical difficulty for the problem posed on the unbounded half line. The kink released by the perturbation from the unstable (or the saddle-node) equilibrium travels to the left from $x = 0$ with speed c_x but never vanishes, such that the heteroclinic solution converges to the opposite saddle-node equilibrium locally uniformly, but not in any translation-invariant norm that one may want to use to establish well-posedness of the equation. The problem is reflected in the presence of essential spectrum in the linearization at the equilibrium $\psi_*(x; c_x)$, stemming from the linearization at the constant η_*,

$$\operatorname{spec}\left(-\partial_x^4 + (1 - 3\eta^2)\partial_x^2 + c_x\partial_x\right) = \{\lambda = -k^4 + (1 - 3\eta^2)k^2 + \mathrm{i}k,\ k \in \mathbb{R}\},$$

which touches the origin at $\lambda = 0$. Similar to the nonlinear considerations in §3, the essential spectrum can be stabilized in exponentially weighted norms

$$\|u(x)\|_\delta = \|u(x)\mathrm{e}^{-\delta x}\|_{L^2(\mathbb{R}^-)}, \qquad \delta \gtrsim 0,$$

but nonlinear analysis is typically not feasible in such norms. It is therefore not clear how the subsequent computer-supported analysis of the saddle-node could be made more rigorous.

We computed an eigenfunction e associated with the kernel at the saddle-node and an associated adjoint eigenfunction e^* to obtain an expansion for an effective equation on a center manifold,

$$A' = \alpha(c_x - c_x^{\mathrm{osn}}) + \beta A^2 + \mathrm{O}\left((c_x - c_x^{\mathrm{osn}})^2 + |c_x - c_x^{\mathrm{osn}}||A| + (|A| + |c_x - c_x^{\mathrm{osn}}|)^3\right), \tag{4.1}$$

where

$$\alpha = \int_{-\infty}^{0} e^*(x)\left(\psi_{\mathrm{cl/d}}(x; c_x^{\mathrm{osn}})\right)_x \mathrm{d}x, \qquad \beta = \int_{-\infty}^{0} e^*(x)\left(3\psi_{\mathrm{cl/d}}(x; c_x^{\mathrm{osn}})e^2(x)\right)_{xx} \mathrm{d}x, \tag{4.2}$$

with normalizations

$$\int_{-\infty}^{0} e^*(x)e(x)\mathrm{d}x = 1, \qquad \int_{-\infty}^{0} e(x)\cdot\exp(x/10)\mathrm{d}x = 1,$$

Note that the second normalization is as usual somewhat arbitrary, fixing the length of the vector $e(x)$ used to coordinatize the center manifold. Since e^* is exponentially localized, all integrals converge, and we find for clamped and Dirichlet boundary conditions, respectively,

$$\alpha_{\mathrm{cl}} = -0.493\ldots, \qquad \beta_{\mathrm{cl}} = -0.0297\ldots, \qquad \alpha_{\mathrm{d}} = -0.959\ldots, \qquad \beta_{\mathrm{d}} = -0.0297\ldots.$$

From the expansion, we compute a leading order passage time near the saddle-node T which gives frequency ω and spacing L of kinks

$$T = \frac{\pi}{\sqrt{\alpha\beta(c_x - c_x^{\mathrm{osn}})}} \quad \omega = 2\sqrt{\alpha\beta(c_x - c_x^{\mathrm{osn}})}, \quad k = \omega/c_x, \quad L = 2\pi/k. \tag{4.3}$$

We compare the predictions with measurements in direct simulations and find agreement, for speeds c_x very close to criticality; see Fig. 10. Agreement is much better for Dirichlet boundary conditions. A tentative explanation for the discrepancy in the clamped case is as follows. The eigenfunction associated with the saddle-node is exponentially localized; see the degeneracy of the saddle-node in Fig. 7. The heteroclinic orbits correspond to global excursions that converge back to this equilibrium, but in a leading direction not associated with this eigenfunction but with continuous spectrum reflecting the slow shedding of a kink. In this sense, the excursion can be understood as a codimension-two heteroclinic loop connecting symmetric saddle-node equilibria, where heteroclinics enter the critical equilibrium along a direction other than the saddle-node, leading to changed asymptotics. Unfortunately, the direction associated with this flip of the heteroclinic is not hyperbolic as in [5] and we are not aware of good heuristics for predicted asymptotics in this case.

On the other hand, the presence of a flip bifurcation usually marks the boundary between a heteroclinic orbit to a saddle-node bifurcation on a limit cycle and a heteroclinic orbit to a hyperbolic equilibrium. For moderate domain sizes and clamped boundary conditions, the limit of time-periodic orbits is indeed a heteroclinic loop to the unstable equilibrium resulting from the saddle-node bifurcation. In particular, one finds a small region of coexistence of periodic orbits and stable equilibria, that is, of wrinkled and oblique stripes; see Fig. 11.

We conclude with a more detailed description of the resulting (time-)periodic orbits in Fig. 12. Solutions converge to stationary solutions of the Cahn-Hilliard equation (in the steady frame) but develop characteristic non-monotone twin-horn structures as transients. It would clearly be interesting to analyze this bifurcation in a more precise asymptotic analysis.

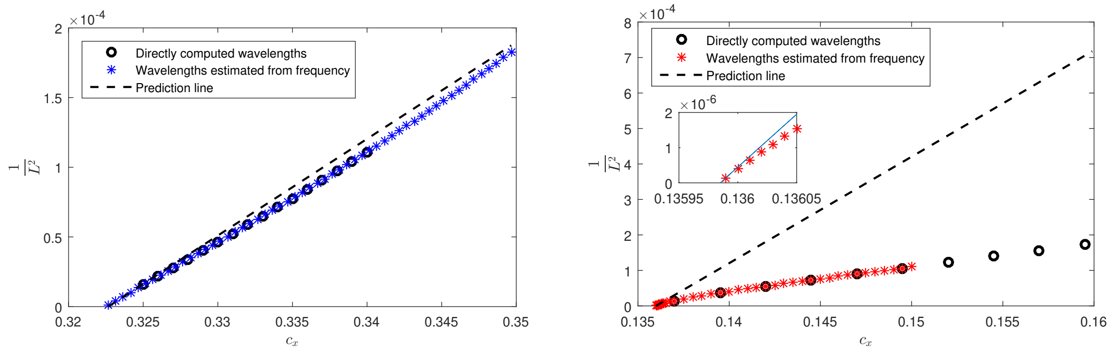

Figure 10. *Plot of L^{-2} from measured data close to c_x^{osn}, compared with the prediction (4.3), for Dirichlet (left) and clamped (right) boundary conditions. Measurements of wavelengths were either direct as L, (○) or indirect through temporal periods $2\pi/\omega$, (∗).*

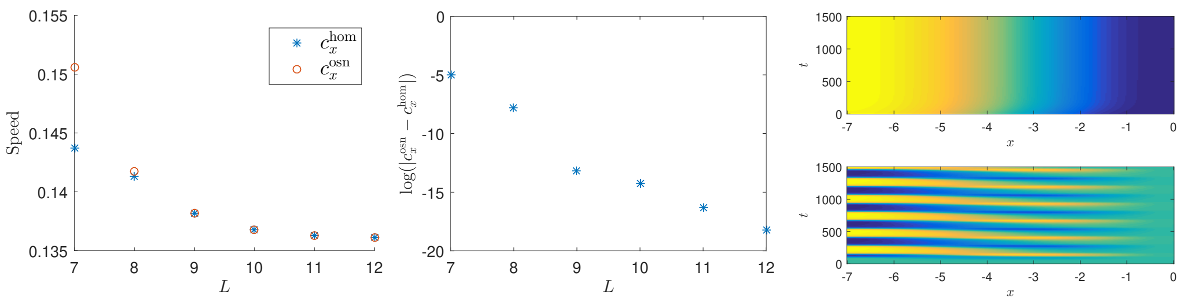

Figure 11. *Critical speeds $c_x^{\mathrm{osn/hom}}$ over moderate sized domains, $L = 7, 8, ..., 12$, for clamped boundary conditions. Left: c_x^{hom} (the speed at which the periodic orbits disappear) and c_x^{osn} (the speed at which the saddle node occurs) versus domain size. Both converge as $L \to \infty$. Middle: $\log(|c_x^{\mathrm{osn}} - c_x^{\mathrm{hom}}|)$ versus domain size, showing that this difference converges to zero exponentially in L. Right: space-time demonstration of bistability for $L = 7, c_x = 0.148$. Initial data for the top right plot was a small perturbation of the equilibrium at the saddle node; ψ maintains the half-heteroclinic profile, corresponding to oblique stripes (see Fig. 5). The bottom right plot used low amplitude random initial data, and converges to a stable periodic orbit.*

4.3. Kink-shedding beyond the saddle-node and detachment. We conclude the study of the Cahn-Hilliard regime with predictions until detachment of zigzags, the upper boundary of the orange region in the left panel of Fig. 4. From direct simulations, we find that the wavelength continuously decreases until the kink-shedding detaches and we relax to $\psi \equiv 0$ as the stable solution. In any bounded domain, this detachment transition induces a very steep bifurcation, common for transitions between convective and absolute instabilities [21, 50, 38]. Speed and wavenumber converge to speed and wavenumber of the invasion front in the Cahn-Hilliard equation, given by [41, Lemma 1.5]

$$c_x^{\mathrm{lin}} = \sqrt{\frac{2}{27}\left(-1+\sqrt{7}\right)}\left(2+\sqrt{7}\right) \sim 1.62208, \qquad k^{\mathrm{lin}} = \frac{3(3+\sqrt{7})}{8\sqrt{5+\sqrt{7}}} \sim 0.765672.$$

The analysis in [15] demonstrates this limiting behavior in the case of the complex Ginzburg-Landau equation and, making conceptual assumptions on existence [41] and transversality

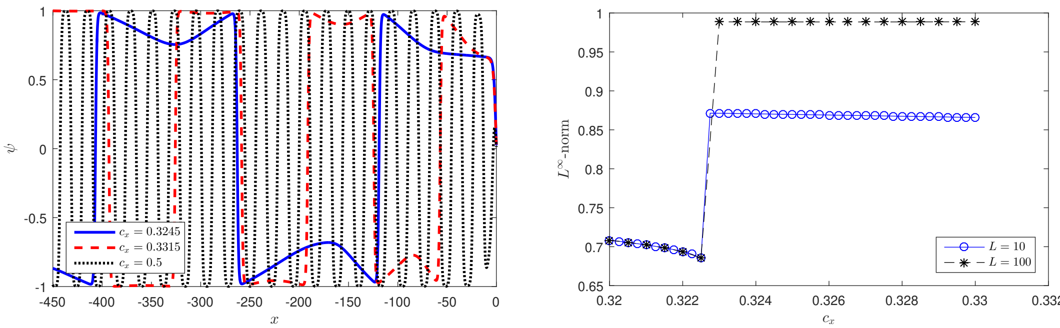

Figure 12. *Profile snapshots (left) from direct simulations for $c_x^{\rm osn} < c_x < c_x^{\rm lin}$ (left), showing characteristic sequences of up-down kinks with decreasing spacing, and a characteristic overshoot in the form of twin-horns at long wave lengths due to the mismatch of the selected angle η at the saddle-node and the value $\eta = \pm 1$ selected by the kink. Twin-horns develop as $x \to -\infty$, as can be seen from a plot of the L^∞-norm of solutions for different domain sizes (right).*

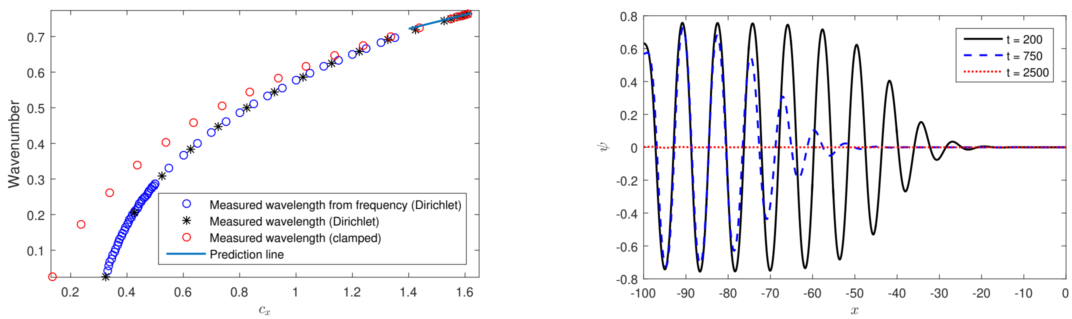

Figure 13. *Measured wavenumber of periodic kink sequences $c_x^{\rm osn} < c_x < c_x^{\rm lin}$, for both Dirichlet and clamped boundary conditions, including predictions from linear spreading speed theory as in (4.4) near $c_{\rm lin}$ (left). Sample solution profiles near detachment (right). Numerical details as in Fig. 12.*

of the Cahn-Hilliard invasion front, should extend to the situation here; see [16] for such a conceptual extension. Moreover, [15] gives a first-order correction to the selected frequency near the linear front speed $c_x^{\rm lin}$ which is independent of the boundary conditions at $x = 0$, obtained simply from the intersection of the absolute spectrum with the imaginary axis. The somewhat lengthy calculation of this intersection yields

$$\begin{aligned} k(c_x) &= \frac{3(3+\sqrt{7})}{8\sqrt{5+\sqrt{7}}} + \frac{9\sqrt{6(2+\sqrt{7})}(4+\sqrt{7})}{800+304\sqrt{7}}(c_x - c_x^{\rm lin}) + \mathrm{O}\left((c_x - c_x^{\rm lin})^{3/2}\right) \\ &\sim 0.765672 + 0.196835(c_x - c_x^{\rm lin}). \end{aligned} \tag{4.4}$$

with good agreement for both clamped and Dirichlet boundary conditions; see Fig. 13.

5. Perpendicular detachment, oblique reattachment, and all-stripe detachment. We next move beyond the regime where the Cahn-Hillard phase approximation gives a good description and use amplitude equations to explore speeds and wavenumbers further away from $k_y = k_{\rm zz}$ and $c_x = 0$; see the right panel of Fig. 4. Indeed, the phase approximation simply predicts stable perpendicular stripes for larger speeds and we will see how instabilities of those correspond to the creation of amplitude defects. Our main focus is the upper boundary of perpendicular stripe existence, the red region in Fig. 4, right panel, in §5.1 and stripe detachment, the upper boundary in Fig. 4 center and right, in §5.2.

5.1. Detachment of perpendicular stripes and reattaching oblique stripes. We study the reattaching of oblique stripes in amplitude equations (2.3),

$$A_t = -(\partial_{xx} + 1 - k_y^2)^2 A + \rho(x)A - 3A|A|^2 + c_x A_x. \tag{5.1}$$

Connections to the Swift-Hohenberg equation can be made more rigorous using spatial center-manifold techniques; see for instance [43, §3] for such a derivation and [42] for the relevant normal form analysis in the presence of a parameter step.

The subspaces $A \in \mathbb{R}$ and $A \in \mathrm{i}\mathbb{R}$ are invariant and correspond to solutions that are even with respect to reflections at $y = 0$ and $y = \pi/k_y$, respectively. Several scalings are possible in this equation and we shall fix throughout $\rho(x) = -\mu\mathrm{sign}(x)$, $\mu = \frac{1}{4}$. Perpendicular stripes in $x < 0$ correspond to solutions $A \equiv const$, oblique stripes to $A \sim \exp(\mathrm{i}k_x x)$.

Continuing perpendicular stripes in c_x: another saddle-node on a limit cycle. Perpendicular stripes can be found as stationary solutions to (5.1) with $A \in \mathbb{R}$, with boundary conditions $A(x) \to 0$ for $x \to \infty$, $A(x) \to r(k_y)$ for $x \to -\infty$, with $r^2(k_y) = \mu - (1 - k_y)^2$. We solved for solutions using numerical continuation and found a saddle-node bifurcation at $c_x^{\mathrm{psn}}(k_y)$ that ends at wavenumbers $k_y = k_y^{\pm}$ with

$$\begin{aligned} k_y^- &\sim 0.781\ldots, & k_y^+ &= \frac{\sqrt{4+\sqrt{3}}}{2} = 1.19709\ldots, \\ c_x^{\mathrm{psn}}(k_y^-) &= 0, & c_x^{\mathrm{psn}}(k_y^+) &= \frac{1}{\sqrt[4]{27}} = 0.43869\ldots \end{aligned} \tag{5.2}$$

see Fig. 14 where the saddle-node is shown in red. We will discuss the rationale for $c_x^{\mathrm{psn}}(k_y^+)$ and expansions for the saddle-node bifurcation for k_y near this upper boundary in §5.2, and analyze the behavior near k_y^- at the end of this section[1]. Continuing through the saddle-node, one can follow the now unstable branch of perpendicular stripes in decreasing c_x and observe phenomena very similar to the kink shedding observed in the Cahn-Hilliard equation, §2. The solution profile develops a kink which separates from the quenching line; see Fig. 14. The kink typically possesses oscillatory tails, and therefore weakly locks to the quenching line, thus leading to a snaking bifurcation diagram near $c_x = 0$, that is, the speed oscillates around 0 while the distance of the kink from the quenching line increases. We emphasize that this kink, while similar to the kinks discussed in §4, is however a kink in the amplitude of the stripe rather than in its orientation.

Interesting phenomena occur when, for smaller k_y, the saddle-node interacts with the snaking diagram. We explore this region in somewhat more detail in §6.2. We see that the

[1] Fig. 14 also shows a light-gray curve that is the continuation of the green spreading speed for smaller values of k_y. For this curve, the speed is in fact complex and we plotted the real part, only. It appears to predict the saddle-node bifurcation surprisingly well, but we were not able to find any theoretical foundation for this apparent coincidence.

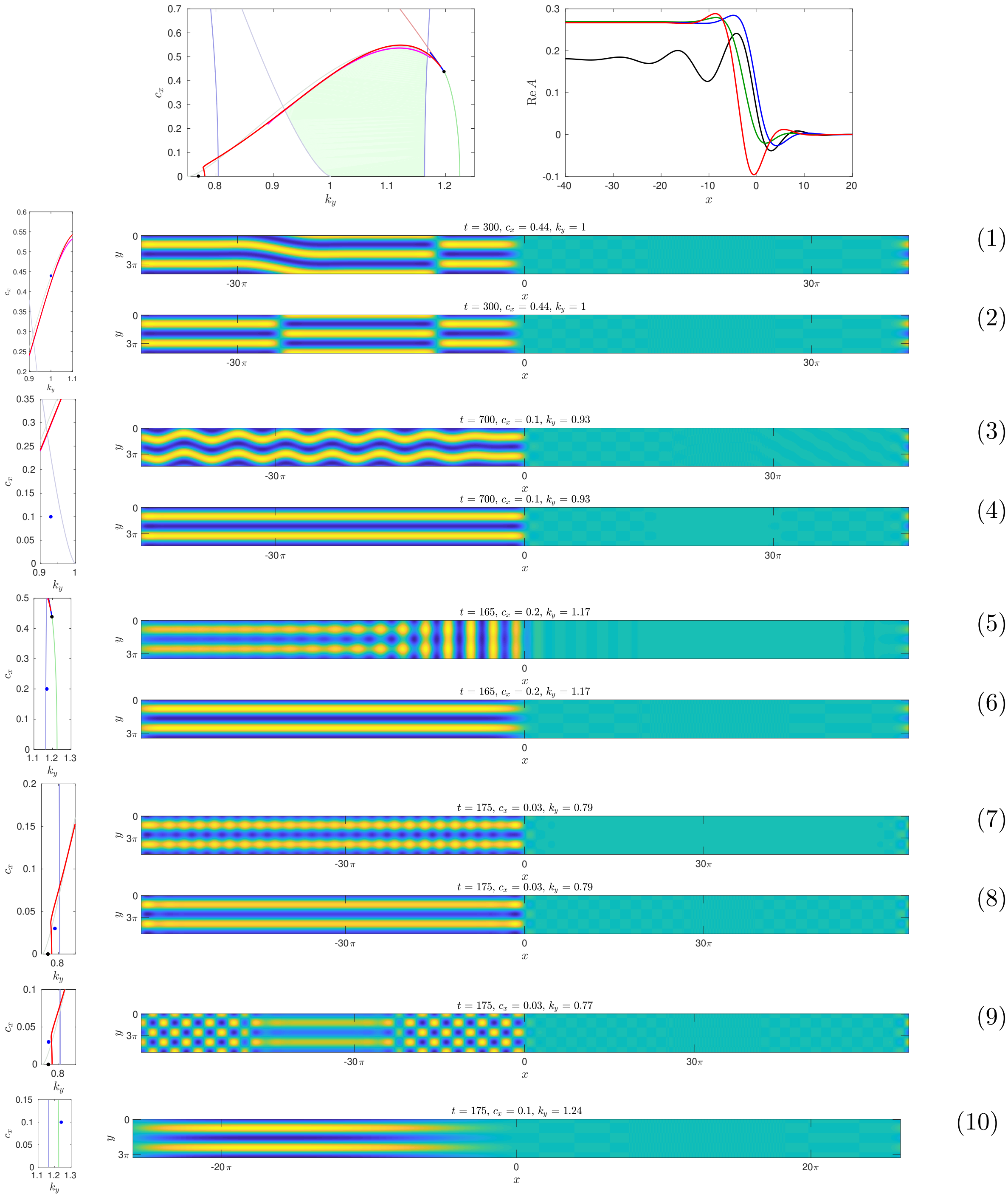

Figure 14. *Bifurcation diagram (top left) for perpendicular stripes in NWS, (5.1); existence bounded by red (saddle-node c_x^{psn}, prediction (5.9) in blue, neighboring pitchfork to oblique in magenta, spreading speed for oblique stripes in brown) and green (perpendicular detachment) curves, with marker at the junction $(k_y^+, c_x(k_y^+))$ (5.2); green shaded stability region bounded by zigzag c_x^{zz} (light gray) and cross-roll $c_x^{\mathrm{cr},\pm}$ (light blue) speeds, marker $(k_y^{\mathrm{t}}, 0)$ for Turing-type instability against amplitude modulations (5.6). Sample plots (top right) for $(k_y, c_x) = (0.781, 0)$ (black), at $(k_y, c_x) = (0.9, 0.05)$ (stable, blue; unstable, red), and $(k_y, c_x) = (0.9, 0.2412)$ at the saddle-node (green). Transitions at boundaries underneath in simulation snapshots; see text for details.*

snaking diagram breaks up into isolas which resemble at first figure-eight shapes with pairs of saddle-nodes. For yet smaller k_y, two saddle-nodes disappear in a cusp bifurcation and only an isola with two saddle-nodes remains, which eventually disappears when the two saddle-node bifurcations coalesce in a parabolic catastrophe at the minimum value of k_y for which perpendicular stripes exist; see Fig. 22. Note that in this respect, the bifurcation diagram in Fig. 14 is rather incomplete, omitting in particular many saddle-node bifurcations near the lower range of k_y-values.

Increasing c_x past the saddle-node, one observes periodic kink-shedding similar to the situation in §2, with some caveats. The kink-shedding is only observed in spaces of functions that are even with respect to $y = 0$ and odd with respect to $y = \pi/2$, or y-translates of functions in this subspace. Perturbations away from this subspace can lead to different phenomenologies, associated with destabilization and bifurcations of perpendicular stripes prior to the saddle-node in the (k_y, c_x)-plane. Those stability boundaries are shown in Fig. 14 and we shall discuss them in somewhat more detail in the remainder of this section. The associated phenomenologies are illustrated in direct simulations for the Swift-Hohenberg, also in Fig. 14 and discussed in more detail, below: We see periodic amplitude-kink shedding for c_x past the saddle-node, with random perturbations (1) and with even in y random perturbations (2), evidencing the saddle-node on a limit cycle dynamics discussed in §5.1; crossing the zigzag boundary near $c_x = 0.1$, zigzag modulations spread into the domain (3); the zigzag instability is suppressed for even initial conditions (4); parallel stripes just past the upper cross-roll instability at $c_x = 0.2$ (5) are suppressed for odd w.r.to $y = \pi/(2k_y)$ initial conditions (6); formation of spotted defects on perpendicular stripes past the lower cross-roll boundary, visible for even initial conditions (7), suppressed for even-odd initial conditions (8), eventually even-odd destabilized to squares past the saddle-node (9); detachment of even-odd perturbations of stripes past the spreading speed of perpendicular stripes (10).

Stability and instability of perpendicular stripes — pitchfork to oblique stripes. The linearization at the quenched perpendicular stripes $A^*(x) \in \mathbb{R}$ exhibits a bifurcation in the direction of complex A, breaking the reflection symmetry in y. We analyzed this bifurcation by studying the linearized operator in the direction of $A_\mathrm{i} := \mathrm{Im}\, A$,

$$\mathcal{L}_\mathrm{i} A_\mathrm{i} = \left[-(\partial_{xx} + 1 - k_y^2)^2 + \rho - 3(A^*)^2\right] A_\mathrm{i}.$$

This operator possesses essential spectrum up to the origin due to the marginal stability of stripes in the far-field. For positive speeds, the essential spectrum can however be pushed into the left half plane using exponential weights $\|A\|_\delta = \sup_x (1 + \exp(-\delta x))^{-1} |A(x)|$, see [10], allowing us to track possible instabilities by eigenvalues emerging near $\lambda = 0$. By gauge invariance (from y-shift symmetry), the operator possesses a zero eigenvalue in this exponentially weighted space, given simply by A^*. Close to the saddle-node, an eigenvalue crosses the origin. At criticality, the zero eigenvalue is a Jordan block of length two and as expected the generalized eigenvector exhibits linear growth at $x \to -\infty$. Spatial dynamics methods as in [37, 39] should allow one to confirm the observed bifurcation towards oblique stripes at this parameter value. We show evidence for this bifurcation in the numerical study of the full Swift-Hohenberg equation in §6.

The corresponding bifurcation curves are shown as the magenta curve in Fig. 14. Bifurcations happen very close to the saddle-node bifurcation except in a region $k_y = 1.12 \pm 0.04$, where the pitchfork is located on the unstable branch just past the saddle-node bifurcation. In this region, perpendicular and oblique quenched stripes coexist, although the oblique stripes, bifurcating from the unstable branch, are unstable against the saddle-node eigenfunction.

Stability and instability of perpendicular stripes – zigzag and cross-roll spreading. We recall from the earlier discussion in the Cahn-Hilliard equation that perpendicular stripes are unstable for small speeds due to an absolute zigzag instability. In the amplitude equation, this instability boundary can be computed from the linear spreading speed associated with the zigzag-instability. Linearizing the amplitude equations at a perpendicular stripe, we find a complex fourth-order linear equation

$$\begin{aligned} A_{\mathrm{r},t} &= [-(\partial_{xx}+1-k_y^2)^2+\mu-9r^2(k_y)]A_{\mathrm{r}},\\ A_{\mathrm{i},t} &= [-(\partial_{xx}+1-k_y^2)^2+\mu-3r^2(k_y)]A_{\mathrm{i}}. \end{aligned}$$

The zigzag instability is visible in the imaginary part. Computing the linear spreading speed of instabilities in this equation [18] one finds

$$c_{\mathrm{zz}}(k_y)=\frac{4}{\sqrt{27}}\left(2+\sqrt{7}\right)\sqrt{\sqrt{7}-1}\left(1-k_y^2\right)^{3/2}, \tag{5.3}$$

which is in fact independent of μ.

The resulting stability boundary is shown in Fig. 14. It intersects the saddle-node bifurcation curve near $k_y = 0.920$, $c_x = 0.278$, thus marking the smallest wavenumber for which there exist quenching rates at which straight perpendicular stripes can be observed.

In a domain of half the width $y \in (0, \pi)$ with Neumann boundary conditions, the zigzag instability is suppressed and perpendicular stripes are stable for smaller values of k_y. A subsequent instability is visible only in the coupled mode system for $Ae^{\mathrm{i}y} + Be^{\mathrm{i}x} + c.c$,

$$\begin{aligned} A_t &= -(\partial_{xx}+1-k_y^2)^2A+\mu A-3A(|A|^2+2|B|^2)+c_xA_x\\ B_t &= 4B_{xx}+\mu B-3B(|B|^2+2|A|^2)+c_xB_x. \end{aligned}$$

Linearizing at $A \equiv \sqrt{\mu-(1-k_y^2)}$, we find a linear operator $4\partial_{xx}+\mu-6(\mu-(1-k_y^2))$ which becomes unstable outside of the interval

$$\left(k_{y_{\mathrm{cr}}}^-, k_{y_{\mathrm{cr}}}^+\right)=\left(\sqrt{1-\sqrt{\mu/2}}, \sqrt{1+\sqrt{\mu/2}}\right)\sim(0.80402, 1.16342)\quad\text{for } \mu=1/4.$$

This instability is known as the cross-roll instability. One readily finds an associated spreading speed [18],

$$c_x^{\mathrm{cr}}(k_y;\mu)=4\sqrt{2\left(1-k_y^2\right)^2-\mu}. \tag{5.4}$$

The upper boundary intersects the pitchfork bifurcation curve near $k_y = 1.168$, $c_x = 0.504$ thus marking the largest wavenumber for which there exist quenching rates for which straight perpendicular stripes can be observed. The resulting stability boundaries are again depicted in

Fig. 14. Phenomena associated with this instability, such as spotted defects on perpendicular stripes, even-odd squares, and parallel stripes, are shown in Fig. 14, (5)–(8)[2].

Both zigzag and cross-roll instability are supercritical in the sense that cubic nonlinearities in associated amplitude equations provide negative feedback and nonlinear saturation. From this one expects [51] and observes numerically that linear spreading speeds give accurate predictions for the associated absolute instability. Both can be eliminated from the Swift-Hohenberg equation in the strip by restricting to even-odd initial conditions.

Blocking perpendicular stripes by amplitude modulations. The saddle-node curve in Fig. 14 terminates at $c_x = 0$ for small k_y, after reaching a minimal value of k_y for finite c_x. There do not appear to be analytic predictions for either minimal k_y-values or the limit at $c_x = 0$ as those appear to be global bifurcations even at these limiting points. The fact that the existence of quenched perpendicular stripes is limited can however be understood near $c_x = 0$ from an amplitude modulational instability. In fact, inspecting the real amplitude equation (5.1) with $\rho(x) \equiv \mu$ at a perpendicular stripe, we find, after shifting $A = r(k_y) + v$ so that the perpendicular stripes correspond to $u = 0$, a Swift-Hohenberg equation with quadratic nonlinearity,

$$(5.5) \qquad v_t = -(\partial_{xx} + 1 - k_y^2)^2 v + \mu_{\text{eff}} v + \gamma v^2 - 3v^3, \qquad \mu_{\text{eff}} = \mu - 9r^2(k_y),\ \gamma = -9r(k_y).$$

This equation undergoes a weakly subcritical pattern-forming instability at $k_y = k_{y,\text{a}}$, with selected wavenumber ℓ_a, with

$$(5.6) \quad k_{y,\text{a}} = \sqrt{1 - \sqrt{2\mu/3}}, \qquad \ell_\text{a} = \sqrt[4]{2\mu/3}, \qquad (k_{y,\text{a}}, \ell_\text{a}) \sim (0.7692, 0.6389) \text{ at } \mu = 1/4.;$$

see Fig. 14 for the location of the amplitude modulational instability relative to the saddle-node. Phenomenologically, perpendicular stripes develop amplitude modulations in this instability.

In the quenched problem with $c_x = 0$, the perpendicular stripes are hyperbolic equilibria prior to this instability, $k_y > k_{y,\text{a}}$. At the instability, they undergo a Hamiltonian Hopf bifurcation with normal form given by a subcritical Ginzburg-Landau equation, $C_{XX} \pm C + C|C|^2 = 0$, after suitable scalings. Stable and unstable manifolds of the origin therefore are contained in compact subsets of a small neighborhood of the origin in the normal form, surrounded by families of invariant tori. Persistence results for such tori under non-normal form perturbations using KAM theory would therefore bound the unstable manifold inside a small neighborhood of the origin and make an intersection with the stable manifold of $A = 0$ at $x = +\infty$ impossible close to criticality.

5.2. Detaching all stripes. Increasing the speed further, one eventually sees all stripes detach: the trivial state occupies an increasingly large region in $x < 0$, behind the quenching line, as c_x increases, until this region eventually expands linearly in time. The quenching process at this point ceases to create stripes and instead creates an unstable state, which is invaded by a free invasion front [51] in a region well separated from the quenching line. We briefly present predictions for this detachment process and, in particular, consequences for stripe orientation.

[2] See also files SH *.M4V in the supplementary materials for movies of solutions

Linear spreading speeds. Disturbances in the linearized Swift-Hohenberg equation with simple y-dependence of the form $\mathrm{e}^{\mathrm{i}k_y y}$ solve

$$u_t = -(\partial_{xx} + 1 - k_y^2)^2 u + \mu u.$$

Compactly supported initial conditions to this equation spread with the spreading speed

$$c_{\mathrm{lin}}(k_y) = \begin{cases} \frac{4\left(2-2k_y^2+\sqrt{1-2k_y^2+k_y^4+6\mu}\right)\sqrt{-1+k_y^2+\sqrt{1-2k_y^2+k_y^4+6\mu}}}{3\sqrt{3}}, & 0 < k_y < \sqrt{\frac{2+\sqrt{3\mu}}{2}} \\ \frac{4\sqrt{-1+k_y^2-\sqrt{4-8k_y^2+4k_y^4-3\mu}}\left(-2+2k_y^2+\sqrt{4-8k_y^2+4k_y^4-3\mu}\right)}{3\sqrt{3}}, & \sqrt{\frac{2+\sqrt{3\mu}}{2}} < k_y < \sqrt{1+\sqrt{\mu}}. \end{cases} \tag{5.7}$$

In a frame moving with this speed, one observes oscillations with frequencies $\omega_{\mathrm{lin}}(k_y)$ which are in $1:1$-resonance with patterns formed at wavenumbers $\omega_{\mathrm{lin}}(k_y) = c_{\mathrm{lin}}(k_y) k_{\mathrm{lin}}(k_y)$, with

$$k_{\mathrm{lin}}(k_y) = \begin{cases} \frac{3\left(3-3k_y^2+\sqrt{1-2k_y^2+k_y^4+6\mu}\right)^{3/2}}{8\left(2-2k_y^2+\sqrt{1-2k_y^2+k_y^4+6\mu}\right)}, & 0 < k_y < \sqrt{\frac{2+\sqrt{3\mu}}{2}} \\ 0, & \sqrt{\frac{2+\sqrt{3\mu}}{2}} < k_y < \sqrt{1+\sqrt{\mu}}. \end{cases} \tag{5.8}$$

We refer to [18] for background and in particular for results that demonstrate that this speed is non-increasing in $|k_y|$ more generally in isotropic systems.

The values for $\mu = 1/4$ are included in Fig. 14 as the upper boundary. The cross-over point $k_y = \sqrt{\frac{2+\sqrt{3\mu}}{2}}$ distinguishes between $k_x = 0$, perpendicular stripes, and $k_x > 0$, oblique stripes, selected by the spreading in the leading edge.

It is worth noticing that, due to the monotonicity $c_{\mathrm{lin}}(k_y) \searrow$ in $k_y > 0$, parallel rolls $(k_y = 0)$ always spread fastest and generic initial conditions in a system without or with fast enough moving parameter step will lead to stripes oriented parallel to the growth interface. In other words, all modes with $k_y \neq 0$ decay pointwise in a window moving in the x-direction with speed $c_{\mathrm{lin}}(k_y = 0)$.

Quenched stripes near the linear spreading speed. Nevertheless, we observed oblique stripes in the quenched system with values of c_x up to the linear spreading speed for values of $k_y \leq 0.95$. For larger values of $k_y \geq 1$, we noticed that oblique stripes selected in the quenching process destabilize against parallel stripes well before the linear spreading speed of oblique stripes in what appears to be related to the cross-roll instability. In fact, for k_y close to the cross-over, the perpendicular stripes are unstable against the cross-roll instability and, by continuity of spreading speeds [18], oblique stripes would be unstable against such perturbations as well for values near the cross-over point. We did not attempt a more comprehensive study of stability of oblique stripes far from the transition near perpendicular stripes.

Near the detachment, the results in [15] establish corrections to the wavenumber based on absolute spectra. Based on these predictions, one concludes in this regime near the linear spreading speed, that the transition from oblique to perpendicular stripes occurs at leading order when the absolute spectrum, computed in the co-moving frame, possesses a triple point at $\lambda = 0$. Some tedious algebra, solving

$$\begin{cases} d(0, \nu; c_x, k_y) = 0, \\ d(0, \nu + \mathrm{i}\ell; c_x, k_y) = 0, \end{cases} \qquad \text{with} \quad d(\lambda, \nu; c_x, k_y) = -(\nu^2 + 1 - k_y^2)^2 + \mu + c_x \nu - \lambda,$$

as one real and one complex equation for the three real variables (ν, ℓ, c_x) with parameter k_y, leads to the location of this triple point at

$$c_{\mathrm{tr}}(k_y) = \frac{4\left(2\sqrt{3}(1-k_y^2) + 5\sqrt{-4(1-k_y^2)^2 + 7\mu}\right)\sqrt{-3(1-k_y^2) + \sqrt{-12(1-k_y^2)^2 + 21\mu}}}{21\sqrt{7}}$$

$$= 2\sqrt{2}\left(\frac{\mu}{3}\right)^{3/4} + 4\sqrt{2+\sqrt{3\mu}}\left(\frac{\mu}{3}\right)^{1/4}\Delta k_y + \mathrm{O}\left(\Delta k_y^2\right), \tag{5.9}$$

for $\Delta k_y = k_y - \sqrt{\frac{2+\sqrt{3\mu}}{2}} \lesssim 0$; see Fig. 14 for a comparison between these asymptotics, the saddle-node of perpendicular stripes, and the pitchfork bifurcation of oblique stripes.

6. Back to Swift-Hohenberg: organizing stripe formation in the moduli space.

We present a conceptually simple object, the moduli space, that captures much of the phenomena presented in this work, in particular many of the results from direct simulations as summarized in the parameter landscape of stripe formation, Fig. 3. The moduli space is a variety in (k_x, k_y, c_x)-space, which encodes stripe formation at the rate c_x with stripes of wave vector (k_x, k_y) in the wake. We present a more precise definition and describe coarse features of this object in §6.1. The remaining paragraphs zoom in on some of the finer structures of the variety, relating to oblique detachment §6.2, perpendicular detachment, §6.3, and the interaction of the two detachments, §6.4. A more detailed description of numerical strategies used for computing this variety is included in the appendix.

6.1. The moduli space.

Solutions that form stripes in the wake of the quenching step can be stationary in an appropriately co-moving frame, hence solving the elliptic traveling-wave equation

$$\begin{aligned} 0 &= -(\partial_{xx} + k_y^2\partial_{yy} + 1)^2 u + \mu(x)u - u^3 + c_x(u_x + k_x u_y), \\ 0 &= \lim_{x\to-\infty}\left(u(x,y) - u_{\mathrm{p}}(k_x x + y; k)\right), \qquad 0 = \lim_{x\to\infty} u(x,y), \qquad u(x,y) = u(x, y+2\pi). \end{aligned} \tag{6.1}$$

Note that the vertical velocity satisfies $c_y = c_x k_x$ since asymptotic patterns are stationary in a stationary frame. We emphasize that this system only captures the *simplest* solutions that form stripes with a given wave vector — actual stripe formation could possess periodic or even more complex temporal modulations. The system (6.1) comes with three parameters (k_x, k_y, c_x), and we define the *moduli space* as

$$\mathcal{M} = \{(k_x, k_y, c_x) | \text{ there exists a solution to (6.1)}\}.$$

One can see using Fredholm theory that this moduli space would typically be a two-dimensional surface, except at singularities (or bifurcation points). Roughly speaking, following [40, 10], the Fredholm index of the linearization at solutions to (6.1) in exponentially weakly localized spaces is given by the signed sum of the number of group velocities associated with neutral or unstable modes pointed towards the quenching line. In our case, the only neutral or unstable mode is associated with the translation of stripes, which possesses zero group velocity in a steady frame, such that its group velocity in the co-moving frame points away from the

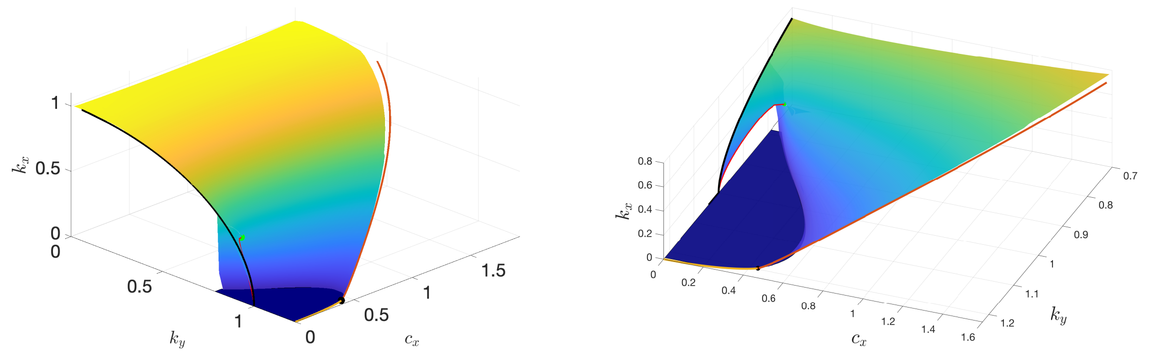

Figure 15. *Left: Coarse view of the moduli space computed via continuation in both k_y and c, with dark blue representing perpendicular stripes, color shading k_x which roughly encodes the angle from perpendicular (dark blue) to parallel (yellow). Right: A zoom into the region $k_y \sim 1$, showing in particular the touch-down near $c_x = 0, k_y = k_{\mathrm{zz}}, k_x = 0$ via the kink-dragging bubble which resembles a delicate arch in this view, the perpendicular stripe detachment at finite c_x^{psn} where a wing-like surface lifts up above the plane, and the hyperbolic catastrophe where delicate arch and wing meet. Perpendicular stripes in dark blue, zig-zag critical stripes with $k_{\mathrm{zz}}^2 = k_x^2 + k_y^2,\ c_x = 0$ as black line, detachment of oblique stripes c_x^{osn} at red curve via kink shedding and at orange curve via final detachment.*

interface, leading to a negative Fredholm index -1, in complete analogy to the calculation in §3. The kernel of the linearization is typically trivial since y-derivatives generated by the translation symmetry are not exponentially localized. As a consequence, the solution surface has codimension 1 in the space of parameters (k_x, k_y, c_x). Practically, this surface encodes the regimes of existence for various orientations of striped patterns formed behind the quenching line. When paired with stability information, it gives a recipe for how to select various orientations of stripes through quenching rates and lateral aspect ratios.

The moduli space is shown in Fig. 15, and various cross-sections in k_y and c_x of the surface are depicted in Fig. 18–21. The two key organizing elements, the oblique detachment and the perpendicular detachment are both clearly recognizable as a delicate arch near $c_x = 0$ and a lift-off to a wing-shaped structure at larger c_x. Both collide in the hyperbolic catastrophe[3]. In the following, we explain in more detail the information contained in this surface, and how it relates to our previous analysis. We encourage, however, at this point, a comparison with the coarse information from the parameter landscape in Fig. 3. The moduli space is computed using a continuation method based on the farfield-core decomposition outlined in [24], as well as in §3.2; see the appendix for more detail about our implementation of this method and how it was used to explore different regions of the surface.

6.2. Kink-dragging and the delicate arch. We next present continuation results of the kink-dragging bubble, visible as the "delicate arch" in Fig. 15. As discussed in §2.4, y-dependent patterned solutions with $c_x = 0$ must select the critical zigzag curve $\{(k_x, k_y, c_x) \mid c_x = 0,\ k_{\mathrm{zz}}^2 = k_x^2 + k_y^2\}$. Indeed starting with $k_x = 0$ and continuing in decreasing k_y with $c_x = 0$ fixed, oblique stripes bifurcated at the zig-zag critical wavenumber $k_y = k_{\mathrm{zz}}$ and the resulting

[3] See movie MODULI.M4V in supplementary materials for an animated 360° tour of the moduli space.

curve conserves the bulk wavenumber $k = k_{zz}$; see the black curve in Fig. 16. These solutions were then used as initial guesses to continue solutions in c_x with k_y fixed (blue curves in Fig. 16, left panel; or Fig. 21, left panel)[4].

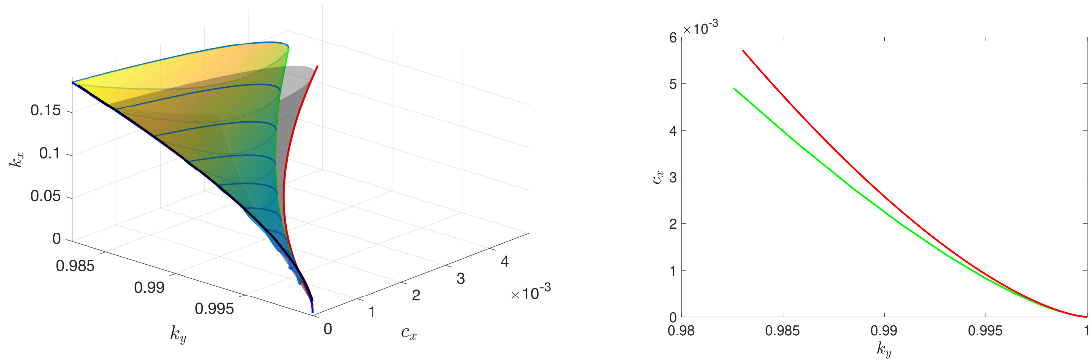

Figure 16. *Top row: Moduli space of the kink-dragging bubble (left) as interpolated surface (colored) from data obtained from numerical continuation for (6.1) in c_x (blue dots), compared against Cahn-Hilliard asymptotics (6.2) with Dirichlet boundary conditions (grey surface). Green and red curves denote the fold curve in Swift-Hohenberg and Cahn-Hilliard respectively. Black curve gives the stationary zig-zag critical curve $\{(k_x, k_y, c_x) : k_{zz}^2 = k_x^2 + k_y^2,\ c_x = 0\}$ discussed in §2.3. Also shown, projection of saddle-node curves onto the (k_y, c_x)-plane (right).*

We also used the bifurcation curves obtained in §4.1 for the kink-dragging bubble in the Cahn-Hilliard system (4.1) to obtain a prediction for the corresponding bubble in Swift-Hohenberg. Letting $(c_{x,ch}, \eta_{ch}(c_{x,ch}))$ denote the bifurcation curves for the speed and angle of stripes in the Cahn-Hilliard system, appropriate scalings yield the Swift-Hohenberg prediction,

$$k_y = k_{\mathrm{zz}} - \zeta, \qquad k_x = \sqrt{2}\, k_{\mathrm{zz}}\, \zeta^{1/2}\, \eta_{\mathrm{ch}}, \qquad c_x = 8\, \zeta^{3/2} c_{x,\mathrm{ch}}; \tag{6.2}$$

see Fig. 16. We find that the numerically predicted saddle-node curve (green) obtained from $(c_{x,\mathrm{ch}}^{\mathrm{osn}}, \eta_{\mathrm{ch}}^{\mathrm{osn}})(\zeta)$, asymptotically agrees well with the saddle-node curve in Swift-Hohenberg (red curve).

6.3. Periodic detachment, oblique reattachment, and all-stripe detachment: the wing.

As predicted in §5.1, continuing perpendicular stripes in c_x for k_y fixed less than $\sqrt{\frac{4+\sqrt{3}}{2}} \sim 1.1971$, the solution destabilizes in a saddle-node bifurcation, after which the unstable branch undergoes a secondary pitchfork bifurcation from which the oblique stripes bifurcate[5]; see Fig. 19. The bifurcating oblique stripes then continue up to the detachment curve $(k_x, k_y, c_x) = (k_{\mathrm{lin}}(k_y), k_y, c_{\mathrm{lin}}(k_y))$ predicted by the linear spreading speed calculated in §5.2. Note that after the fold bifurcation, the perpendicular stripes develop a phase-kink in the vertical direction (see solution (3) of Fig. 19), indicating how the nearby periodic solutions will evolve as shown

[4]See KINK_KY9.930188E-01.M4V in supplementary materials for movie solutions along a slice of the bubble.
[5]See MOVIE_KY1.064602E+00.M4V in supplementary materials for video of how solutions vary along this slice of moduli space

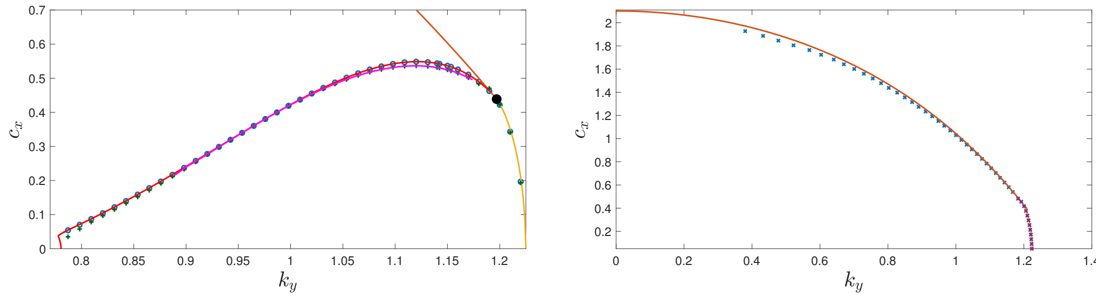

Figure 17. *Left: Comparison of the pitchfork and saddle-node curves found in Swift-Hohenberg (blue and green points) with predictions from Newell-Whitehead-Segel, Fig. 14 (magenta and red curves). Also plotted is the perpendicular stripe detachment curve (yellow) and the projection of the oblique stripe detachment curve (orange). Right: Plot of numerical detachment points (i.e. where the core solution dropped below a certain max norm near the boundary of the far-field) for both oblique (blue x's) and perpendicular (purple x's) stripes against the corresponding predictions from the linear spreading* $c_{\mathrm{lin}}(k_y)$ *for both* $k_y < \sqrt{\frac{2+\sqrt{3\mu}}{2}}$ *(orange curve) and* $k_y > \sqrt{\frac{2+\sqrt{3\mu_0}}{2}}$ *(yellow curve).*

in Fig. 14. Fig. 17 compares the saddle-node, pitchfork, and detachment points, to the corresponding predictions from previous sections.

6.4. Hyperbolic and elliptic catastrophes at detachment interaction. Also, our solutions show that some reattachment curves near the lower k_y boundary of the perpendicular attachment regime actually bend back and connect with the critical zigzag curve at $c_x = 0$, with the solution developing a kink at its interface[6]; see Fig. 21. This happens when the kink-dragging bubble merges with the oblique-stripe reattachment surface, causing the top branch of the kink-dragging bubble to continue to the all-stripe detachment curve and the bottom branch of the bubble to connect with the perpendicular stripes. Locally, the reconnection can be described by Morse theory as a family of *hyperbolas* forming a hyperboloid, $\delta k_y \sim \kappa_1^2 - \kappa_2^2$ where κ_j are local coordinates in the (k_x, c_x)-plane.

Meanwhile, the saddle-node curve of perpendicular stripes reaches a minimum near $k_y \sim 0.777$ before snaking around $c_x = 0$; see Fig. 14. Towards these smaller k_y-values, perpendicular stripes are confined to a finite interval of c_x-values where they form an isola between the two branches of the saddle-node, before disappearing. Near the singularity, the isolas have the shape of *ellipses*, forming a paraboloid, $\delta k_y \sim \kappa_1^2 + \kappa_2^2$ for local coordinates κ_j in the $(c_x, \|w\|)$-plane.

Increasing k_y slightly from this elliptic singularity, $k_y \sim 0.778$, we observe two new saddle-nodes emerging in a cusp singularity and the isolas form figure-eight shaped curves; see Fig. 22. We also found a small branch of oblique stripes with $k_x \sim 0$ which bifurcates off and reattaches to the upper branches of the figure-eight isolas[7]; see Fig. 23. We suspect that the isolas continue into a more complex scenario of broken up snakes and ladders as observed for instance

[6]See Catastrophe_ky8.42e-01.m4v and Catastrophe_ky8.4712e-01.m4v in supplementary materials for movies of how solutions vary around the catastrophe.

[7]See barba_ky7.8e-01.m4v in supplementary materials for movie of solutions along this isola.

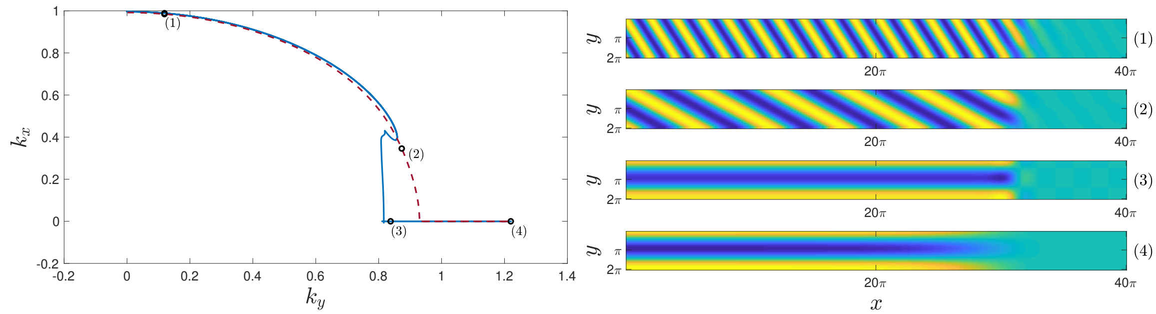

Figure 18. *Slices of the moduli space $c_x = 0.2949$ (left, dotted red) and 0.0908 (left, solid blue) fixed with solution profiles at various points along the surface (right)*

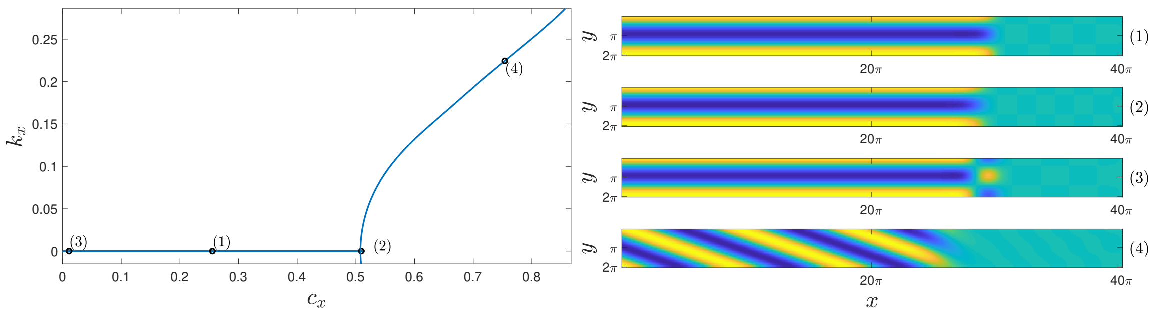

Figure 19. *Cross-section of the moduli space for $k_y = 1.0646$ fixed, near the oblique stripe reattachment point (left), with solution profiles along the perpendicular and oblique curves (right). Profiles (1) and (2) lie on the stable branch of the fold while (3) lies on the unstable branch.*

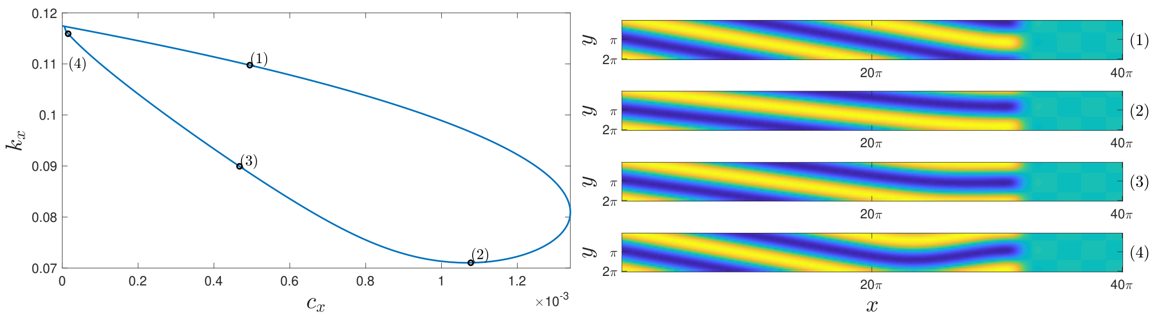

Figure 20. *Cross section of kink-dragging bubble, continuation data with $k_y = 0.99302$ fixed (left) and solution profiles for points along kink-dragging curve (right), corresponding to labels in the left figure.*

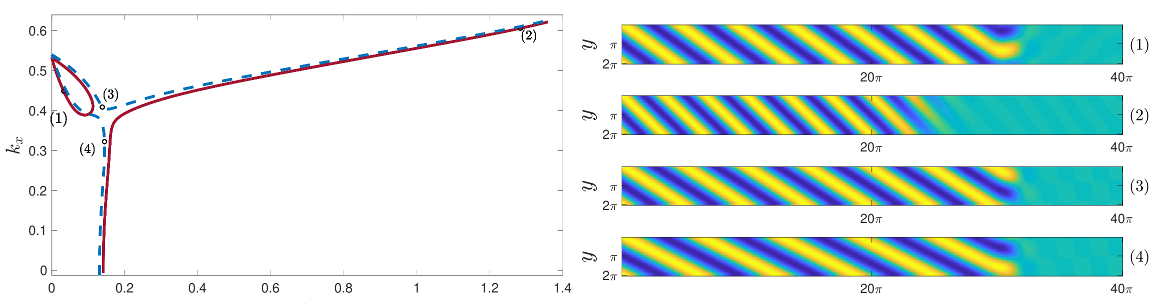

Figure 21. *Catastrophe where kink-dragging bubble merges with the oblique reattachment surface as k_y is decreased (left). Cross-sections on left for $k_y = 0.84712$ (solid dark red), and $k_y = 0.842$ (dashed blue) and corresponding solution profiles (right).*

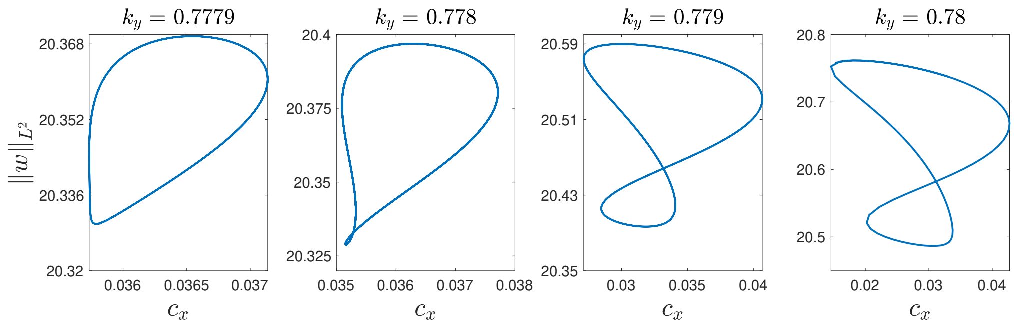

Figure 22. *Isola curves of perpendicular stripes near the parabolic catastrophe, plotting L^2-norm of the core-solution against c_x, for $k_y = 0.7779, 0.778, 0.779, 0.78$ (from left to right).*

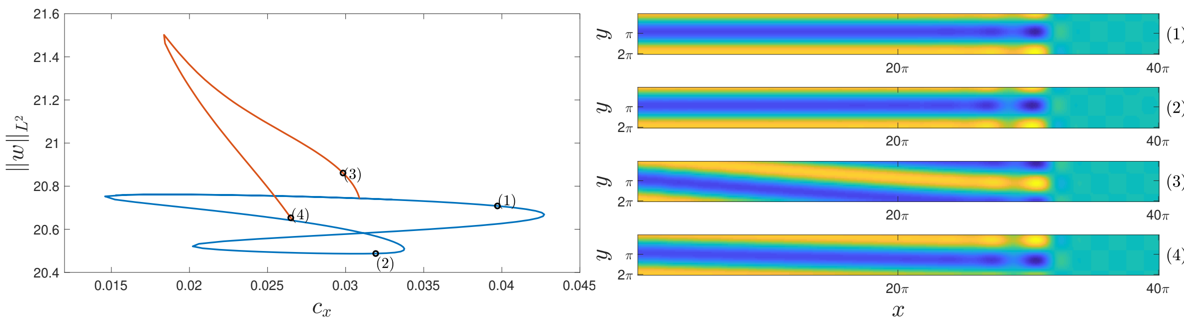

Figure 23. *Perpendicular figure-eight isola (blue) for $k_y = 0.78$, where a small branch of oblique stripes ($\max k_x \sim 0.12$) bifurcate as secondary pitchfork bifurcations (orange) .*

in [26, 25].

7. Discussion. We analyzed the formation of stripes formed in the wake of a directional quenching process, relating in particular orientation and wavelength to the speed of propagation of the quenching line. Our work here focused on a region of transition between stripes formed perpendicular to the quenching line, and stripes formed at a small oblique angle. Our major findings illustrate that this transition is in fact quite subtle, organized by a variety of bifurcations of solutions, often accompanied by essential spectra.

While we present ample numerical evidence substantiating our predictions, more rigorous results would clearly be desirable. We believe that approximation results for traveling waves connecting the quenched Swift-Hohenberg problem and Cahn-Hilliard or Newell-Whitehead-Segel equations should allow one to lift many of the results in §3–5 to the Swift-Hohenberg model. More substantial insight is needed for predictions based on spreading speeds, which suffer from the fundamental lack of understanding of invasion processes absent a comparison principle; see for instance [18] for a review.

Among the key organizing recurring features are saddle-node bifurcations. Taking a perspective of increasing the rate of quenching c_x for a fixed lateral wavenumber k_y, we can continue both perpendicular and oblique stripes until they undergo a saddle-node bifurcation. In both cases, the saddle-node bifurcation marks the release of a defect (or kink) from the quenching line. This kink is visible both in the continuation of the unstable branch from the saddle-node bifurcation point, as its distance from the quenching line increases with decreasing quenching speed c_x, and in the profiles visible for speeds past the critical saddle-node speed. Both saddle-node bifurcations are of independent theoretical interest. First, the bifurcation to periodic orbits resembles in many ways a saddle-node on a limit cycle, with many caveats reflected in the asymptotics of period and in the lack of an actual homoclinic orbit connecting the saddle-node equilibrium. Second, it would be very desirable to gain a theoretical understanding of the saddle-node that would ideally predict its location in the (c_x, k_y)-plane, possibly also explain the presence of the additional nearby pitchfork bifurcation for perpendicular stripes. Our analysis only gives such predictions near a detachment point and for small speeds, only.

Beyond the transition from perpendicular to oblique stripes, we have analyzed detachment [15, 16], $k_y \sim 0$ [14], and $k_y = 0$, $c_x \sim 0$ [13] in prior work. From this "completist" perspective, the major challenge appears to be a description of the moduli space in a vicinity of $k_y, c_x = 0$.

Our results are somewhat universal. Small speed predictions near the zigzag transition should hold quite universally for systems with such an instability. Moderate speed predictions should hold near onset, where amplitude equation approximations are valid. We did notice however subtle differences varying μ or, more generally, setting $\rho(x) = \mu_\pm$ for $\pm x > 0$. From this perspective, we hope that our computational approach in §6 will help compare different systems systematically and quantitatively, in particular in regimes where subtle bifurcations and multi-stability make a direct mapping of parameter space through direct simulations unreliable. Interesting extensions here would include different types of parameter triggers, boundary conditions at $x = 0$ rather than quenching, and non-variational effects, but also systems such as reaction-diffusion models from morphogenesis, possibly far from onset.

Our results on perpendicular stripes in §5 predicted transitions in direct simulations very well. In particular, the far-field instabilities of perpendicular stripes appeared to be the only limitations on observability other than the saddle-node and pitchfork bifurcations. We did not attempt such a stability analysis for oblique stripes, which would be both algebraically and computationally more involved, but would clearly complement and to some extent complete the analysis, here.

Within the context of pattern formation, a very natural next question would point towards growth patterns when spots, in particular on hexagonal lattices, are the preferred states. Many of the tools here, in particular computational recipes from §6 and amplitude equation approximations would still be available in this context. Changes in orientation of hexagonal lattices with respect to the quenching line are however subject to more complex pinning effects, as the lateral period for the creation of ideal energy-minimizing hexagons would be subject to a wealth of resonances as the relative angle varies; we refer to [32] for a study of hexagonal patterns formed in the wake of interfaces, with emphasis on periodicities and orientation of lattices in the example of phyllotaxis.

Appendix A. Farfield-Core continuation and the moduli space. To explore the moduli space, we use the general approach outlined in [24], as well as in §3.2, where heteroclinic profiles are decomposed into a pure asymptotic state cut off away from negative infinity, and an exponentially localized perturbation which glues the asymptotic state to another asymptotic state at positive infinity. We use a cutoff function $\chi_-(x)$ supported on $x \leq d+1$ with $\chi_- \equiv 1$

on $x \le d$ to decompose solutions of (6.1) as

$$u(x,y) = w(x,y) + \chi_-(x)u_{\mathrm{p}}(k_x x + y; k);$$

see Fig. 24 for a depiction of the various solution components.

We insert this Ansatz into (6.1) and use the fact that the stripe solution u_{p} is an easily available solution for $\rho \equiv \mu$ to obtain the following nonlinear problem for $(w; k_x, k_y, c_x)$ on a truncated domain

$$\mathcal{L}\left(w + \chi_- u_{\mathrm{p}}\right) - \left(w + \chi_- u_{\mathrm{p}}\right)^3 = 0, \qquad (x,y) \in (0, L_x) \times (0, 2\pi) \tag{A.1}$$

$$w = w_{xx} = 0, \qquad (x,y) \in \{0, L_x\} \times (0, 2\pi) \tag{A.2}$$

$$\partial_y^j w(x,0) - \partial_y^j w(x, 2\pi) = 0, \qquad x \in (0, L_x), j = 0, ..., 3, \tag{A.3}$$

$$\int_{x=0}^{2\pi} \int_{y=0}^{2\pi} u_{\mathrm{p}}'(k_x x + y; k) w(x,y) \mathrm{d}y \, \mathrm{d}x = 0, \tag{A.4}$$

$$-\left(k^2 \frac{d^2}{d\xi^2} + 1\right)^2 u_{\mathrm{p}} + \mu u_{\mathrm{p}} - u_{\mathrm{p}}^3 = 0, \qquad \xi \in (0, 2\pi) \tag{A.5}$$

$$\frac{d^j}{d\xi^j} u_{\mathrm{p}}(0) - \frac{d^j}{d\xi^j} u_{\mathrm{p}}(2\pi) = 0, \qquad j = 0, ..., 3. \tag{A.6}$$

where $\mathcal{L} = -(\partial_{xx} + k_y^2 \partial_{yy} + 1)^2 + \rho(x) + c_x(\partial_x + k_x \partial_y)$, and $k^2 = k_x^2 + k_y^2$, and where the parameter jump is now located at $L_{\mathrm{q}} = 8L_x/10$, $\rho(x) \sim -\mu \mathrm{sign}(x - L_{\mathrm{q}})$.

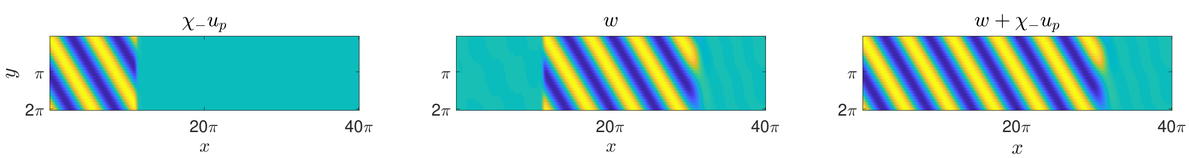

Figure 24. *Example of a farfield-core decomposition of a traveling wave solution $u = w + \chi_- u_{\mathrm{p}}$, quenching interface at $x = 8L_x/10 \sim 100$ and far-field cutoff at $x = 3L_x/10 \sim 37$.*

This decomposition suppresses the continuous family of neutral modes, arising from the asymptotic periodic pattern, in the spectrum of the linearization about a generic traveling wave solution $u(x,y)$ of (6.1). In the x-unbounded domain, one imposes exponential weights on the perturbation w to obtain a Fredholm index -1 linearization in w which, after appending the wavenumber parameter k_x, yields a Fredholm index 0 problem, with trivial kernel whenever the derivative with respect to k_x does not belong to the range.

Truncating to $x \in [0, L_x]$, we impose Dirichlet boundary conditions in x which are readily found to be transverse to the unstable subspace of the asymptotic stripes and constant state at $x = \pm\infty$. This implies that the truncated problem has the correct Fredholm index in (w, k_x, k_y, c_x) and the perturbation w will be exponentially localized in the domain for generic parameter values. This also implies that truncated solutions converge to the full modulated traveling wave as $L_x \to \infty$. Note also that since the quenching interface destroys x-translational invariance, we need only one phase condition (A.4) to eliminate the multiplicity from the translational mode $\partial_y u_{\mathrm{p}}$ and fix the vertical phase of the solution. See [24, 31] for more details about this approach.

Using the above formulation, we implemented an arc-length continuation algorithm in MATLAB2018A, solving for (w, k_x) and continuing in either c or k_y with the other fixed. We roughly followed the approach outlined in [24, §3] and refer the reader there for more details on the implementation. To discretize the problem, we used fourth-order finite differences in x with $L_x = 40\pi$ and approximately 500 grid points. We used a pseudo-spectral discretization in y with 26 collocation points and the far-field periodic patterns u_p were also computed on a periodic domain $\zeta \in [0, 2\pi)$ using a Fourier pseudo-spectral method with 26 collocation points. The quenching interface was placed at $x = 8L_x/10$ and the cutoff-interface was placed at $d = 3L_x/10$; see Fig. 24 for a depiction of the computational domain and the solution decomposition. The Jacobian of the discretized system is formed explicitly in w while the derivatives in parameters were approximated using a second-order finite difference. We used the trust-region algorithm in MATLAB's FSOLVE to perform the nonlinear Newton iterations. Our initial guess for the nonlinear solver consisted of a piece-wise constant stripe solution, rotated to have a specific wavenumber, and cutoff at the quenching interface. Throughout all of this section we used the onset parameter $\mu = 0.25$.

We explored the solution space starting from initial guesses along the line $(k_x, k_y) = (1, 0)$, keeping $c \in (0, c_\mathrm{lin}(0))$ fixed and continuing in k_y to track oblique solutions as they continuously perturbed from parallel stripes, $k_y = 0$. For large k_y curves in parameter space either run into the detachment curve predicted by $c_\mathrm{lin}(k_y)$ (roughly in the region $c_x \geq .55$) or the solution transitions, via a pitchfork bifurcation, through the family of perpendicular stripes, to the opposite orientation of stripes with $k_x < 0$. In the former cases, the core solution w loses localization, bleeding into the far-field domain $x \in (0, d)$ and the L^2-norm of the full solution u decays to zero as $c_x \to c_\mathrm{lin}(k_y)$.

To explore the perpendicular stripe region we started from initial patterns along the line $(k_x, k_y) = (0, 1.12)$ for a range of c_x. Continuing in increasing k_y for $c_x < c_\mathrm{lin}\left(\sqrt{\frac{2+\sqrt{3\mu}}{2}}\right) \sim 0.438691$, the core solution once again loses localization as the detachment curve $c_\mathrm{lin}(k_y)$ is approached. For larger $c_x \sim 0.5$, continuation in k_y gives an isola bounded by the two saddle-node curves predicted by the Newell-Whitehead-Segel equation; see Fig. 14 and 17.

Fig. 15 combines these two sets of continuations, oblique/parallel and perpendicular striped, to give an overview of the moduli surface and we find good agreement for all orientations of stripes between the measured detachment points and predictions from the linear spreading speed (5.7); see Fig. 18–21 for slices of the moduli space for select values of c_x with corresponding solution profiles[8].

REFERENCES

[1] S. Akamatsu, S. Bottin-Rousseau, and G. Faivre. Experimental evidence for a zigzag bifurcation in bulk lamellar eutectic growth. *Phys. Rev. Lett.*, 93:175701, Oct 2004.

[2] E. Ben-Jacob, I. Cohen, and H. Levine. Cooperative self-organization of microorganisms. *Advances in Physics*, 49(4):395–554, 2000.

[3] E. Bodenschatz, W. Pesch, and G. Ahlers. Recent developments in Rayleigh-Bénard convection. *Annual*

[8]See MOVIE_C2.948980E-01.M4V and MOVIE_C9.081633E-02.M4V in supplementary materials for movies of these solutions.

Review of Fluid Mechanics, 32(1):709–778, 2000.

[4] A. S.-H. Chen and S. W. Morris. On the origin and evolution of icicle ripples. *New Journal of Physics*, 15(10):103012, 2013.

[5] S.-N. Chow and X.-B. Lin. Bifurcation of a homoclinic orbit with a saddle-node equilibrium. *Differential Integral Equations*, 3(3):435–466, 1990.

[6] A. Doelman, B. Sandstede, A. Scheel, and G. Schneider. The dynamics of modulated wave trains. *Mem. Amer. Math. Soc.*, 199(934):viii+105, 2009.

[7] D. Double. Imperfections in lamellar eutectic crystals. *Materials Science and Engineering*, 11(6):325 – 335, 1973.

[8] W.-P. Düll. Validity of the Cahn-Hilliard approximation for modulations of slightly unstable pattern in the real Ginzburg-Landau equation. *Nonlinear Anal. Real World Appl.*, 14(6):2204–2211, 2013.

[9] N. Fenichel. Geometric singular perturbation theory for ordinary differential equations. *J. Differential Equations*, 31(1):53–98, 1979.

[10] B. Fiedler and A. Scheel. Spatio-temporal dynamics of reaction-diffusion patterns. In *Trends in nonlinear analysis*, pages 23–152. Springer, Berlin, 2003.

[11] E. M. Foard and A. J. Wagner. Survey of morphologies formed in the wake of an enslaved phase-separation front in two dimensions. *Phys. Rev. E*, 85:011501, Jan 2012.

[12] R. Friedrich, G. Radons, T. Ditzinger, and A. Henning. Ripple formation through an interface instability from moving growth and erosion sources. *Phys. Rev. Lett.*, 85:4884–4887, Dec 2000.

[13] R. Goh, R. Beekie, D. Matthias, J. Nunley, and A. Scheel. Universal wave-number selection laws in apical growth. *Phys. Rev. E*, 94:022219, Aug 2016.

[14] R. Goh and A. Scheel. Pattern-forming fronts in a Swift-Hohenberg equation with directional quenching parallel and oblique stripes. *Journal of the London Mathematical Society*, 98(1):104–128.

[15] R. Goh and A. Scheel. Triggered fronts in the complex Ginzburg Landau equation. *J. Nonlinear Sci.*, 24(1):117–144, 2014.

[16] R. Goh and A. Scheel. Pattern formation in the wake of triggered pushed fronts. *Nonlinearity*, 29(8):2196–2237, 2016.

[17] M. Haragus and A. Scheel. Interfaces between rolls in the Swift-Hohenberg equation. *Int. J. Dyn. Syst. Differ. Equ.*, 1(2):89–97, 2007.

[18] M. Holzer and A. Scheel. Criteria for pointwise growth and their role in invasion processes. *J. Nonlinear Sci.*, 24(4):661–709, 2014.

[19] R. B. Hoyle. *Pattern formation*. Cambridge University Press, Cambridge, 2006. An introduction to methods.

[20] M. Hărăguş-Courcelle and G. Schneider. Bifurcating fronts for the Taylor-Couette problem in infinite cylinders. *Z. Angew. Math. Phys.*, 50(1):120–151, 1999.

[21] M. H. Köpf and U. Thiele. Emergence of the bifurcation structure of a Langmuir–Blodgett transfer model. *Nonlinearity*, 27(11):2711, 2014.

[22] A. L. Krause, V. Klika, T. E. Woolley, and E. A. Gaffney. Heterogeneity induces spatiotemporal oscillations in reaction-diffusion systems. *Phys. Rev. E*, 97:052206, May 2018.

[23] A. Krekhov. Formation of regular structures in the process of phase separation. *Phys. Rev. E*, 79:035302, Mar 2009.

[24] D. J. B. Lloyd and A. Scheel. Continuation and bifurcation of grain boundaries in the Swift-Hohenberg equation. *SIAM J. Appl. Dyn. Syst.*, 16(1):252–293, 2017.

[25] E. Makrides and B. Sandstede. Predicting the bifurcation structure of localized snaking patterns. *Phys. D*, 268:59–78, 2014.

[26] S. McCalla and B. Sandstede. Snaking of radial solutions of the multi-dimensional Swift-Hohenberg equation: a numerical study. *Phys. D*, 239(16):1581–1592, 2010.

[27] I. Melbourne and G. Schneider. Phase dynamics in the real Ginzburg-Landau equation. *Math. Nachr.*, 263/264:171–180, 2004.

[28] A. Mielke. Instability and stability of rolls in the Swift–Hohenberg equation. *Communications in Mathematical Physics*, 189(3):829–853, Nov 1997.

[29] D. G. Míguez, M. Dolnik, A. P. Muñuzuri, and L. Kramer. Effect of axial growth on Turing pattern formation. *Phys. Rev. Lett.*, 96:048304, Feb 2006.

[30] S. A. Mollick, D. Ghose, P. D. Shipman, and R. Mark Bradley. Anomalous patterns and nearly defect-free

ripples produced by bombarding silicon and germanium with a beam of gold ions. *Applied Physics Letters*, 104(4):043103, 2014.

[31] D. Morrissey and A. Scheel. Characterizing the effect of boundary conditions on striped phases. *SIAM Journal on Applied Dynamical Systems*, 14(3):1387–1417, 2015.

[32] M. F. Pennybacker, P. D. Shipman, and A. C. Newell. Phyllotaxis: Some progress, but a story far from over. *Physica D: Nonlinear Phenomena*, 306:48 – 81, 2015.

[33] L. M. Pismen. *Patterns and interfaces in dissipative dynamics*. Springer Series in Synergetics. Springer-Verlag, Berlin, 2006. With a foreword by Y. Pomeau.

[34] J. D. M. Rademacher, B. Sandstede, and A. Scheel. Computing absolute and essential spectra using continuation. *Phys. D*, 229(2):166–183, 2007.

[35] J. Robbin and D. Salamon. The spectral flow and the Maslov index. *Bulletin of the London Mathematical Society*, 27(1):1–33, 1995.

[36] B. Sandstede and A. Scheel. Absolute and convective instabilities of waves on unbounded and large bounded domains. *Phys. D*, 145(3-4):233–277, 2000.

[37] B. Sandstede and A. Scheel. Essential instabilities of fronts: bifurcation, and bifurcation failure. *Dyn. Syst.*, 16(1):1–28, 2001.

[38] B. Sandstede and A. Scheel. Basin boundaries and bifurcations near convective instabilities: a case study. *J. Differential Equations*, 208(1):176–193, 2005.

[39] B. Sandstede and A. Scheel. Hopf bifurcation from viscous shock waves. *SIAM J. Math. Anal.*, 39(6):2033–2052, 2008.

[40] B. Sandstede and A. Scheel. Relative Morse indices, Fredholm indices, and group velocities. *Discrete Contin. Dyn. Syst.*, 20(1):139–158, 2008.

[41] A. Scheel. Spinodal decomposition and coarsening fronts in the Cahn-Hilliard equation. *J. Dynam. Differential Equations*, 29(2):431–464, 2017.

[42] A. Scheel and J. Weinburd. Wavenumber selection via spatial parameter jump. *Philos. Trans. Roy. Soc. A*, 376(2117):20170191, 20, 2018.

[43] A. Scheel and Q. Wu. Small-amplitude grain boundaries of arbitrary angle in the Swift-Hohenberg equation. *ZAMM Z. Angew. Math. Mech.*, 94(3):203–232, 2014.

[44] G. Schneider. Validity and limitation of the Newell-Whitehead equation. *Mathematische Nachrichten*, 176(1):249–263.

[45] R. Sheth, L. Marcon, M. F. Bastida, M. Junco, L. Quintana, R. Dahn, M. Kmita, J. Sharpe, and M. A. Ros. Hox genes regulate digit patterning by controlling the wavelength of a Turing-type mechanism. *Science*, 338(6113):1476–1480, 2012.

[46] A. Stegner and J. E. Wesfreid. Dynamical evolution of sand ripples under water. *Phys. Rev. E*, 60:R3487–R3490, Oct 1999.

[47] J. Swift and P. C. Hohenberg. Hydrodynamic fluctuations at the convective instability. *Phys. Rev. A*, 15:319–328, Jan 1977.

[48] T. Teramoto, X. Yuan, M. Bär, and Y. Nishiura. Onset of unidirectional pulse propagation in an excitable medium with asymmetric heterogeneity. *Phys. Rev. E*, 79:046205, Apr 2009.

[49] S. Thomas, I. Lagzi, F. Molnár Jr, and Z. Rácz. Probability of the emergence of helical precipitation patterns in the wake of reaction-diffusion fronts. *Physical Review Letters*, 110(7):078303, 2013.

[50] S. M. Tobias, M. R. E. Proctor, and E. Knobloch. Convective and absolute instabilities of fluid flows in finite geometry. *Phys. D*, 113(1):43–72, 1998.

[51] W. van Saarloos. Front propagation into unstable states. *Physics Reports*, 386(2):29 – 222, 2003.

[52] Wilczek, M., Tewes, W. B.H., Gurevich, S. V., Köpf, M. H., Chi, L. F., and Thiele, U. Modelling pattern formation in dip-coating experiments. *Math. Model. Nat. Phenom.*, 10(4):44–60, 2015.